# A Compressible Model for the Simulation of Moist Mountain Waves

DALE R. DURRAN[1] AND JOSEPH B. KLEMP

*National Center for Atmospheric Research,[2] Boulder, CO 80307*

(Manuscript received 21 March 1983, in final form 2 August 1983)

ABSTRACT

A two-dimensional, nonlinear, nonhydrostatic model is described which allows the calculation of moist airflow in mountainous terrain. The model is compressible, uses a terrain-following coordinate system, and employs lateral and upper boundary conditions which minimize wave reflections.

The model's accuracy and sensitivity are examined. These tests suggest that in numerical simulations of vertically propagating, highly nonlinear mountain waves, a wave absorbing layer does not accurately mimic the effects of wave breakdown and dissipation at high levels in the atmosphere. In order to obtain a correct simulation, the region in which the waves are physically absorbed must generally be included in the computational domain (a nonreflective upper boundary condition should be used as well).

The utility of the model is demonstrated in two examples (linear waves in a uniform atmosphere and the 11 January 1972 Boulder windstorm) which illustrate how the presence of moisture can influence propagating waves. In both cases, the addition of moisture to the upstream flow greatly reduces the wave response.

## 1. Introduction

Although mountain waves have been the subject of extensive study, most previous theoretical work has neglected the effects of moisture on the dynamics of these waves. This is apparently not a critical omission, since the results from dry mountain wave theory have been successfully used to explain qualitatively most of the features in observed waves. Nevertheless, the presence of extensive cloudy regions can significantly affect the wave dynamics, since the structure of mountain waves is strongly dependent on the atmospheric stability, and that stability is greatly reduced wherever the atmosphere is saturated. Barcilon *et al.* (1979) noted that the stability reduction produced in low-level clouds could decrease the mountain wave drag to as little as one half the dry value. Durran and Klemp (1982a) found that changes in upstream moisture can significantly modify the structure and amplitude of trapped mountain lee waves.

The primary impediment to the study of moist mountain waves is the complexity of the equations which govern moist flow. It is very difficult to obtain analytic solutions to these equations if the moist processes are approximated in a realistic manner. As a result, most previous studies have relied on a very idealized treatment of the moist processes. The simplest such idealization was employed by Smith and Lin (1982), who obtained linear analytic wave solutions for fixed heating and cooling functions based on observed rainfall rates. Since the heating and cooling are prespecified, there is no explicit relation between latent heat release and the condensation rate; indeed the calculated streamlines often show descent in the heating regions. Thus, although this approach can provide valuable information about the interaction between thermal and orographic forcing, it cannot be easily used to produce self-consistent solutions for actual moist flows.

The influence of moisture can also be introduced through its effect on the stability, without explicitly calculating latent heating and cooling rates. As noted by Lalas and Einaudi (1974) and Durran and Klemp (1982b), the linear wave equation has exactly the same form in both dry and saturated environments provided that the Brunt–Väisälä frequency is suitably adjusted to reflect the influence of moisture. Thus, in principle one could include the effects of condensation and evaporation by solving the dry equations for an atmosphere in which the cloudy regions are replaced by dry regions of suitably reduced stability. Fraser *et al.* (1973) and Barcilon *et al.* (1979) have used this approach to determine the effects of reversible condensation on linear hydrostatic mountain waves. Barcilon *et al.* (1980) used a similar procedure to study the case of completely irreversible condensation by assuming that all downdrafts are unsaturated so that cloudiness (and low stability) is limited to regions of upward displacement and upward motion. One of the significant advantages to this type of approach is that the linear solution can be obtained analytically whenever the

[1] Present affiliation: Department of Meteorology, University of Utah, Salt Lake City, UT 84112.

[2] The National Center for Atmospheric Research is sponsored by the National Science Foundation.

mean state is sufficiently simple. On the other hand, if the mean state does not permit analytic solutions, this approach is considerably less attractive. An additional complication arises in specifying the cloud boundaries, which are determined by the wave structure, and therefore are not known *a priori*. In order to obtain a self-consistent flow, Barcilon *et al.* (1979) used a numerical iteration scheme to match the cloud boundaries with regions of upward displacement.

A third approach has been followed by Durran and Klemp (1982a), who used a computer model to numerically integrate the equations of motion governing the flow of moist air over a topographic barrier. The numerical modeling approach allows the investigator to study a wide variety of situations which are not amenable to analytic solution (i.e., nonlinear, nonhydrostatic, or time dependent waves produced by nonuniform wind, temperature and humidity soundings over terrain of arbitrary shape), and, in particular, it allows a more accurate treatment of the moist processes.

The purpose of this paper is to provide a detailed description of the mountain wave model used in Durran and Klemp (1982a), to document its verification, and to demonstrate its utility by presenting calculations showing some effects of moisture on propagating mountain waves. In Section 2, we present the physical equations and boundary conditions used in the model, and their numerical formulation. The model's accuracy and sensitivity are examined in Section 3. In Section 4, we present examples which show that the presence of moisture can have a significant impact on the dynamics of idealized and observed mountain waves.

## 2. Formulation of the numerical model

### a. Model equations

The model is designed to calculate the two-dimensional airflow over an infinitely long, uniform mountain barrier. The Coriolis force is neglected, since we will consider only high Rossby number flows over narrow mountains. Under these assumptions, the momentum, pressure, thermodynamic and moisture equations may be written in the following form:

$$\frac{du}{dt} + c_p\theta_M \frac{\partial \pi}{\partial x} = D_u, \tag{1}$$

$$\frac{dw}{dt} + c_p\theta_M \frac{\partial \pi}{\partial z} = g\frac{\theta_M - \bar{\theta}_M}{\bar{\theta}_M} + D_w, \tag{2}$$

$$\frac{d\pi}{dt} + w\bar{\Pi}_z + \frac{R}{c_v}(\bar{\Pi} + \pi)\left(\frac{\partial u}{\partial x} + \frac{\partial w}{\partial z}\right) - \frac{R}{c_v}\frac{(\bar{\Pi} + \pi)}{\theta_v}\frac{d\theta_v}{dt} = 0, \tag{3}$$

$$\frac{d\theta}{dt} = M_\theta + D_\theta, \tag{4}$$

$$\frac{dq_v}{dt} = M_{q_v} + D_{q_v}, \tag{5}$$

$$\frac{dq_c}{dt} = M_{q_c} + D_{q_c} \tag{6}$$

$$\frac{dq_r}{dt} = M_{q_r} + D_{q_r}, \tag{7}$$

where

$$\frac{d}{dt} = \frac{\partial}{\partial t} + u\frac{\partial}{\partial x} + w\frac{\partial}{\partial z},$$

and

$$\theta_v = \theta(1 + 0.61q_v), \quad \theta_M = \theta_v(1 - q_c),$$
$$\bar{\Pi} + \pi = \left(\frac{p}{p_0}\right)^{R/c_p} = \left(\frac{R}{p_0}\rho\theta_M\right)^{R/c_v}. \tag{8}$$

In the above, $p$ is the pressure, $p_0 = 1000$ mb, $\rho$ the total density, $R$ the gas constant for dry air, $c_p$ the specific heat of dry air at constant pressure, $c_v$ the specific heat at constant volume, $L$ the latent heat of vaporization, $\theta$ the potential temperature, and $u$ and $w$ are the horizontal and vertical velocity components. The mixing ratios of water vapor, cloud water, and rain water are $q_v$, $q_c$, and $q_r$. The terms $D$ and $M$ contain the contributions from subgrid scale mixing and cloud microphysics. Overbars denote the undisturbed horizontally homogeneous mean state.

The cloud microphysics are included through a Kessler parameterization and are identical to those used in the convective cloud model of Klemp and Wilhelmson (1978). The terms which represent the microphysics are presented in detail in the Appendix. Subgrid scale turbulence is parameterized as a function of the larger scale flow via a first-order closure formulation which depends on the relative strengths of stratification and shear (Lilly, 1962). The details of this parameterization may also be found in the Appendix.

### b. Terrain following coordinate transformation

Since mountain lee waves are forced by the irregularities in the earth's surface, it is very important to accurately represent the terrain in the model. This is most easily accomplished when the mountain profile coincides with a coordinate surface. The following transformation of the vertical coordinate (Gal-Chen and Somerville, 1975) is used to map the lowest coordinate surface to an irregular lower boundary

$$\zeta = \frac{z_t(z - z_s)}{z_t - z_s}. \tag{9}$$

In this equation, $z_s(x)$ is the terrain elevation, and $z_t$ the depth of the model domain.

The basic model equations may be written in transformed form as

1) Horizontal momentum equation

$$\frac{\partial u}{\partial t} + u\frac{\partial u}{\partial x} + (Gu + Hw)\frac{\partial u}{\partial \zeta} + c_p\theta_M\left(\frac{\partial \pi}{\partial x} + G\frac{\partial \pi}{\partial \zeta}\right) = D_u. \quad (10)$$

2) Vertical momentum equation

$$\frac{\partial w}{\partial t} + u\frac{\partial w}{\partial x} + (Gu + Hw)\frac{\partial w}{\partial \zeta} + c_p\theta_M H\frac{\partial \pi}{\partial \zeta} = g\frac{(\theta_M - \bar{\theta}_M)}{\bar{\theta}_M} + D_w. \quad (11)$$

3) Pressure equation

$$\frac{\partial \pi}{\partial t} + u\frac{\partial \pi}{\partial x} + (Gu + Hw)\frac{\partial}{\partial \zeta}(\bar{\Pi} + \pi) + \frac{R}{c_v}(\bar{\Pi} + \pi) \times\left(\frac{\partial u}{\partial x} + G\frac{\partial u}{\partial \zeta} + H\frac{\partial w}{\partial \zeta}\right) - \frac{R}{c_v}\frac{(\bar{\Pi} + \pi)}{\theta_v}\frac{d\theta_v}{dt} = 0. \quad (12)$$

4) Thermodynamic equation

$$\frac{\partial \theta}{\partial t} + u\frac{\partial \theta}{\partial x} + (Gu + Hw)\frac{\partial \theta}{\partial \zeta} = M_\theta + D_\theta. \quad (13)$$

5) Moisture equations

$$\frac{\partial q_v}{\partial t} + u\frac{\partial q_v}{\partial x} + (Gu + Hw)\frac{\partial q_v}{\partial \zeta} = M_{q_v} + D_{q_v}, \quad (14)$$

$$\frac{\partial q_c}{\partial t} + u\frac{\partial q_c}{\partial x} + (Gu + Hw)\frac{\partial q_c}{\partial \zeta} = M_{q_c} + D_{q_c}, \quad (15)$$

$$\frac{\partial q_r}{\partial t} + u\frac{\partial q_r}{\partial x} + (Gu + Hw)\frac{\partial q_r}{\partial \zeta} = M_{q_r} + D_{q_r}, \quad (16)$$

where

$$\left.\begin{aligned} G &= \frac{\partial \zeta}{\partial x} = \frac{\zeta - z_t}{z_t - z_s}\frac{\partial z_s}{\partial x} \\ H &= \frac{\partial \zeta}{\partial z} = \frac{z_t}{z_t - z_s} \end{aligned}\right\}. \quad (17)$$

*c. Finite differencing for the compressible equations of motion*

Equations (10)–(16), which govern the dynamics of mountain waves are compressible, and therefore include sound waves. While the sound waves are not meteorologically significant, they travel at high speeds and thus severely limit the time step in explicit numerical integration schemes. In order to remove this computational burden, many researchers have chosen the anelastic equations, which do not admit sound waves, as the basis for their models. However, the anelastic system requires the solution of a Poisson equation for the pressure at each time step, and when a coordinate transformation is present, the Poisson solution procedure becomes less efficient because the transformation complicates the coefficient structure of the pressure equation.

We have adopted an alternate approach which retains the fundamental prognostic equation for pressure, and appears to be at least as computationally efficient as the anelastic approach. In this technique (Klemp and Wilhelmson, 1978), the sound wave modes are integrated separately, with a smaller time step than that used for the other processes of meteorological interest. Although all the terms in Eqs. (10)–(16) have some influence on sound waves, only the pressure gradient terms in the momentum equations and divergence terms in the pressure equation are responsible for rapid sound wave propagation. Therefore, in the two time step approach, the pressure gradient and divergence terms are linearized, and (10)–(12) are rewritten as follows.

$$u_t + c_p\bar{\theta}_M(\pi_x + G\pi_\zeta) = f_u, \quad (18)$$

$$w_t + c_p\bar{\theta}_M H\pi_\zeta = f_w, \quad (19)$$

$$\pi_t + \frac{\bar{c}^2}{c_p\bar{\rho}\bar{\theta}_M^2}[\bar{\rho}\bar{\theta}_M(u_x + Gu_\zeta) + H(\bar{\rho}\bar{\theta}_M w)_\zeta] = f_\pi, \quad (20)$$

where

$$\bar{c}^2 = \frac{c_p}{c_v}R\bar{\Pi}\bar{\theta}_M.$$

The remaining terms, which are not responsible for rapid sound wave propagation (advection, buoyancy, subgrid-scale mixing, and the nonlinear parts of the divergence and pressure gradient terms) are collected in $f_u$, $f_w$, and $f_\pi$.

If the time derivatives were approximated by ordinary leapfrog differencing, all the other terms in Eqs. (18)–(20) would be evaluated at the middle time level and used to advance the integration between $t - \Delta t$ and $t + \Delta t$ in a single step. In the two time step approach, the terms which comprise $f_u$, $f_w$, and $f_\pi$ are evaluated in exactly that manner, but the integration between $t - \Delta t$ and $t + \Delta t$ no longer occurs in a single step. Instead, it is advanced by several smaller time steps of length $\Delta\tau$, during which the left-hand sides of Eqs. (18)–(20) are continuously updated. The length of the small time step is chosen to guarantee the stability of the sound waves. The large time step is chosen to ensure stable and accurate integration of the meteorologically significant processes. The integration of the thermodynamic and moisture equations is not affected by sound waves, so these equations (which are differenced in the standard leapfrog manner) will not be included in this discussion.

It should be emphasized that the purpose of the two time step technique is to treat the sound wave modes in a stable manner. Efficiency in the small time step calculations is achieved at the expense of accuracy in the sound wave modes themselves, but, since the sound waves are not believed to be meteorologically signif-

icant, they need not be accurately integrated. The gravity wave modes are still accurately computed.

The small time step stability requirement (Courant–Friedrichs–Lewy condition) is $\bar{c}\Delta\tau/(\Delta x^2 + \Delta z^2)^{1/2} < 1$. In mountain wave modeling, $\Delta x$ is typically much larger than $\Delta z$, so extra efficiency can be achieved by making the small time step implicit in the vertical. The finite difference representation of the small time step equations, with the coordinate transformation included, is

$$\delta_\tau u + c_p\bar{\theta}_M(\delta_x\pi^\tau + G\delta_{2\zeta}\overline{\pi^\tau}^x) = f_u^t, \quad (21)$$

$$\delta_\tau\tilde{w} + c_p\bar{\rho}\bar{\theta}_M^2 H\overline{\delta_\zeta\pi}^\tau = \bar{\rho}\bar{\theta}_M f_w^t, \quad (22)$$

$$\delta_\tau\pi + \frac{\bar{c}^2}{c_p\bar{\theta}_M}\delta_x u^{\tau+\Delta\tau} + \overline{G\delta_{2\zeta}u^{\tau+\Delta\tau}}^x + \frac{\bar{c}^2}{c_p\bar{\rho}\bar{\theta}_M^2}H\overline{\delta_\zeta\tilde{w}}^\tau = f_\pi^t, \quad (23)$$

where the spatial finite difference operators are defined as

$$\delta_{n\xi}\phi(\xi) = (1/n\Delta\xi)[\phi(\xi + n\Delta\xi/2) - \phi(\xi - n\Delta\xi/2)], \quad (24)$$

$$\overline{\phi(\xi)}^{n\xi} = \frac{1}{2}\phi(\xi + n\Delta\xi/2) + \phi(\xi - n\Delta\xi/2), \quad (25)$$

and a time average is defined

$$\overline{\phi(\tau)}^\tau = \frac{1+\epsilon}{2}\phi(\tau + \Delta\tau) + \frac{1-\epsilon}{2}\phi(\tau), \quad (26)$$

and $\tilde{w} = \bar{\rho}\bar{\theta}_M w$. For computational efficiency, only those vertical differences which remain in the limit of flat terrain are treated implicitly. Since $G \ll H$ for most realistic terrain profiles, the length of the small time step is usually not significantly restricted by the explicit treatment of the vertical differences introduced by the coordinate transformation.

In the original Klemp–Wilhelmson formulation the parameter $\epsilon$ is zero, in which case the time differencing is Crank–Nicolson which is unconditionally stable. However, this alone is not adequate to ensure the stability of the entire big-step small-step integration cycle. A weak instability was encountered in the sound wave modes while simulating mountain waves in deep, very stable environments. This was eliminated by adjusting $\epsilon$. When $0 < \epsilon \leqslant 1$ the scheme is unconditionally stable, and in addition it slowly damps the sound wave modes. Tests were run comparing the effects of different values of $\epsilon$ on the mountain wave solutions. A value of $\epsilon = 0.2$ was sufficient to completely eliminate the sound wave instability without perceptibly influencing the gravity waves. The gravity waves are not affected because they change very slowly over a single small time step.

In the large time step, the time differencing is leapfrog, horizontal advection is fourth order, and vertical advection is second order. Buoyancy, diffusion and coordinate transformation terms are computed to at least second-order accuracy. The microphysics are included through a two-step procedure proposed by Soong and Ogura (1973). In the first step, the temperature and moisture variables are advected and diffused; in the second step, they are adjusted to the correct thermodynamic balance. The details of the large time step finite differencing are given in the Appendix.

### *d. Boundary conditions*

The ground is the only physical boundary associated with the mountain wave problem. We require the normal velocity to vanish at the surface

$$w = u\frac{\partial z_s}{\partial x} \quad \text{at} \quad \zeta = 0. \quad (27)$$

As a result $Gu + Hw = 0$ at $\zeta = 0$, so the vertical flux terms in (10)–(16) vanish at the lower boundary. The subgrid scale mixing terms also require additional boundary conditions at the surface. All mixing normal to the boundary is assumed to vanish at the boundary point, which prevents the mean state vertical gradients from being distorted by mixing near the ground.

The radiation boundary condition, which requires that all energy transport be directed out of the domain, is approximated at the upper boundary. This condition is crucial for the successful simulation of vertically propagating mountain waves. There are, however, physical situations in which downward propagating waves reflect from sharp gradients in the atmospheric structure or regions of wave overturning and breakdown and have a significant impact on the wave dynamics below. In such instances the correct solution can be obtained only by applying this boundary condition above the reflecting layers.

The radiation boundary condition is approximated by adding an absorbing layer to the top of the domain.[3] The effective mean viscosity in the absorber is chosen so that waves entering from below have negligible amplitude when they arrive at the top of the absorbing layer where the actual boundary condition is $w = 0$. Reflections, which might otherwise be produced by vertical variations in the viscosity, are minimized by ensuring that the strength of the absorber increases gradually with height. These requirements impose a

[3] A new radiation upper boundary condition (Klemp and Durran, 1983), in which the pressure at the upper boundary is determined from the Fourier transformed vertical velocity, has recently been incorporated in this model. It appears to improve significantly the model efficiency without sacrificing accuracy. However, since the model results we published earlier (Durran and Klemp, 1982a) were obtained using an absorbing layer, and since we wish to discuss the model's sensitivity to the upper boundary using the simpler and more thoroughly understood absorbing layer formulation, the simulations described in this paper do not use this new radiation boundary condition.

constraint on the minimum depth of an effective wave absorbing layer. Klemp and Lilly (1978) have suggested that, for linear hydrostatic waves, this minimum depth is approximately one vertical wavelength.

Both viscous and Rayleigh damping have been used in absorbing layers (Clark, 1977; Klemp and Lilly, 1978). Rayleigh damping has been chosen for this model because the second derivatives required for viscous damping have a complicated finite difference structure in the presence of the coordinate transformation. In the absorbing layer, only the perturbations of a variable from its upstream value are damped. The damping terms, which are added to the right-hand sides of the $u$, $w$ and $\theta$ equations, are

$$\left.\begin{aligned} R_u &= \tau(z)(u-\bar{u}) \\ R_w &= \tau(z)w \\ R_\theta &= \tau(z)(\theta-\bar{\theta}) \end{aligned}\right\}. \tag{28}$$

The damping coefficient has the structure

$$\tau(z) = \begin{cases} 0, & \text{for} \quad z \leqslant z_D \\ -\dfrac{\alpha}{2}\left(1-\cos\dfrac{z-z_D}{z_T-z_D}\pi\right), & \text{for} \quad 0 \leqslant \dfrac{z-z_D}{z_T-z_D} \leqslant \dfrac{1}{2} \\ -\dfrac{\alpha}{2}\left[1+\left(\dfrac{z-z_D}{z_T-z_D}-\dfrac{1}{2}\right)\pi\right], & \text{for} \quad \dfrac{1}{2} \leqslant \dfrac{z-z_D}{z_T-z_D} \leqslant 1, \end{cases} \tag{29}$$

where $z_D$ is the height of the bottom of the absorbing layer and (in this instance only) $\pi$ is 3.1416. Klemp and Lilly (1978) have shown that for a single, linear hydrostatic wave, an absorbing layer with a sinusoidal vertical viscosity profile will be most effective when $\alpha$ satisfies $2 \leqslant \alpha/k\bar{u} \leqslant 5$ where $k$ is the horizontal wavenumber. In actual simulations, $\alpha$ is chosen so that the dominant horizontal wavenumbers are absorbed most efficiently.

The lateral boundary conditions are also designed to radiate energy out of the domain. The actual boundary condition is again chosen to minimize the spurious reflection of an outward propagating wave when it encounters the lateral boundary. Our approach is a variant of the procedure suggested by Orlanski (1976), in which the phase speed $c$ of a gravity wave impinging on the boundary is estimated, and the flow variables are advected out the boundary at the speed $u + c$. If the phase speed is correctly chosen the gravity wave will pass through the boundary with minimal reflection.

Several authors have suggested modifications to the original Orlanski scheme (e.g., Klemp and Lilly, 1978; Klemp and Wilhelmson, 1978; Clark, 1979; Miller and Thorpe, 1981), which differ primarily in their specification of $c$, and the number of variables to which this boundary condition is applied. Several of those modifications have been tested in this model; a scheme similar to that described by Klemp and Lilly (1978) appeared to produce the best overall results in a variety of numerical tests. In this approach the speed of propagation is estimated by averaging $u + c$ vertically along the lateral boundaries. At each vertical level, $u + c$ is estimated according to the original prescription of Orlanski (1976), except that the result is bounded by zero, and the maximum speed for which the numerical time step is stable. Without loss of generality we consider the right boundary, at which the speed of propagation is estimated as

$$(u+c)^t = \sum_{k=1}^{N} \min\left[u_{\max}, \max\left(0, \frac{\Delta x}{\Delta t}\frac{u^{t-\Delta t}_{b-1,k} - u^t_{b-1,k}}{u^{t-\Delta t}_{b-1,k} - u^{t-\Delta t}_{b-2,k}}\right)\right], \tag{30}$$

where $u_{\max}$ is the magnitude of the fastest propagation speed for which the numerical time step is stable, and $b$ is the index of the right boundary point. Klemp and Lilly (1978) have shown that it is better to overestimate the magnitude of $u + c$ than to underestimate it; thus we have biased the calculation toward an outward directed phase speed by setting any inward directed phase speeds to zero prior to averaging. Then the horizontal velocity field at the boundary is updated on the small time step as follows:

$$u^{\tau+\Delta\tau}_{b,k} = u^\tau_{b,k} - \frac{(u+c)^t \Delta\tau}{\Delta x}(u^\tau_{b,k} - u^\tau_{b-1,k}). \tag{31}$$

This boundary condition is not applied to the other fields, which, because of the mesh staggering, require only a boundary condition on the horizontal advection terms. At outflow boundaries, $w$, $\pi$, and the sum $(q_v + q_c)$ are held fixed ($q_r$ is zero at inflow), while the term $u\partial\theta/\partial x$ is estimated as follows. The full thermodynamic equation may be written:

$$\frac{\partial\theta}{\partial t} + u\frac{\partial\theta}{\partial x} + f = 0, \tag{32}$$

where vertical advection and diabatic terms are collected in $f$. A one-dimensional wave of uniform am-

plitude traveling at a propagation speed estimated by (30) will satisfy

$$\frac{\partial\theta}{\partial t} + (u + c)\frac{\partial\theta}{\partial x} = 0. \tag{33}$$

Equating (32) and (33) yields an estimate of $\partial\theta/\partial x$, so that the form of (32) actually solved at the boundary becomes

$$\frac{\partial\theta}{\partial t} + \left(1 + \frac{u}{c}\right)f = 0. \tag{34}$$

Note that for a stationary disturbance, $c = -u$ and $\partial\theta/\partial t = 0$. This treatment of the inflow boundary condition on $\theta$ is similar to that proposed by Klemp and Lilly (1978).

*e. Model initialization and numerical smoothing*

A small amount of numerical smoothing is applied to all fields (except $\pi$) throughout the domain, to control the growth of nonlinear instability and filter out short wavelength modes, whose behavior cannot be accurately represented by finite difference schemes. The smoother is equivalent to a fourth-order damper. Its numerical form is

$$\gamma[\phi_{i+2} + \phi_{i-2} - 4(\phi_{i+1} + \phi_{i-1}) + 6\phi_i]; \tag{35}$$

$\gamma$ has a nominal value of 0.015 in the horizontal and 0.001 in the vertical. A second order smoother is used at grid points adjacent to the boundaries with a coefficient that matches the interior smoothing for $2\Delta x$ scale disturbances. No smoothing is performed at boundary points. The smoother is applied only to the perturbations of the variables from their values in the undisturbed upstream flow. In the absorbing layer, the horizontal smoothing coefficient gradually increases with height to 0.0625, the value at which $2\Delta x$ waves are completely removed each time step. The horizontal smoothing coefficient is increased in the wave absorbing layer to improve the short wavelength absorption because Rayleigh damping attenuates short wavelengths less efficiently than long wavelengths. The damping of short wavelength disturbances in the wave absorbing layer is further enhanced by applying a second-order smoother to the pressure distribution along the topmost grid level.

The vertical smoothing coefficient is so small that its influence is restricted primarily to the $2\Delta z$ waves. The horizontal smoothing coefficient is large enough to produce some damping in several of the shortest wavelengths. In order to estimate the impact of the horizontal smoother, we consider its impact on a steady linear hydrostatic wave in a Boussinesq atmosphere. The vertical structure of this wave will be proportional to

$$\exp\left[i\frac{k_p N}{k_a \bar{u}}\left(1 + \frac{i\gamma^* k_s^4}{\bar{u}k_a}\right)z\right], \tag{36}$$

where $\gamma^*$ is the dimensional smoothing coefficient, and $k_a$, $k_p$ and $k_s$ are the numerical representations of the horizontal wavenumbers from the advection, pressure gradient and smoothing terms, respectively. With the staggered mesh and fourth-order advection used in this model, the damping experienced by an upward radiating wave is

$$\exp\left[\frac{-2N\gamma^*\Delta x}{\bar{u}^2\Delta t}\frac{\left(\sin\frac{k\Delta x}{2}\right)(6 + 2\cos 2k\Delta x - 8\cos k\Delta x)}{(\tfrac{4}{3}\sin k\Delta x - \tfrac{1}{6}\sin 2k\Delta x)^2}z\right]. \tag{37}$$

Thus, at a height of one half vertical wavelength ($N\pi/\bar{u}$), a $4\Delta x$ wave decays to 47% of its value at the surface. Over the same depth, a $10\Delta x$ wave, which in this model is the approximate visual scale of the mountain, retains 95% of its amplitude, while a $30\Delta x$ wave, which is the scale at which the linear mountain forcing is strongest, retains 99.8%.

The impact of this smoother on the calculated flow fields and momentum flux was evaluated in linear and weakly nonlinear cases (for which no numerical smoothing is needed) by performing identical simulations with and without smoothing, and comparing the solutions. The differences were negligible. Even in the momentum flux, which is a second-order quantity, they were confined to the third decimal place.

Leapfrog time differencing allows the solutions at odd and even time steps gradually to diverge. This is prevented by the time-smoothing scheme

$$\left.\begin{aligned}\phi_*^{t+\Delta t} &= \phi^{t-\Delta t} + 2\Delta t F_*^t \\ \phi^t &= \phi_*^t + \eta(\phi_*^{t+\Delta t} - 2\phi_*^t + \phi^{t-\Delta t})\end{aligned}\right\}. \tag{38}$$

Terms which have not yet been time-smoothed are denoted by an asterisk; $\eta$ is 0.2. The first equation represents a standard leapfrog step; the second, the time-smoothing. This technique has been analyzed by Asselin (1972), who found that it strongly damped the computational mode without significantly affecting the physical mode. The smoothing, applied at every time step, has a gentler influence on the solution than

schemes which rely on one application of a strong filter or an Euler time step in a cycle with a large number of unsmoothed steps.

## 3. Model verification

In order to verify the model's ability to simulate mountain wave flows we will examine its behavior in three test cases. In the first two cases, we compare the model results with analytic solutions; in the third, we compare the model simulation of the 11 January 1972 wind-storm in Boulder, Colorado, with data and previous simulations by different models.

### *a. Linear hydrostatic waves in an isothermal atmosphere*

The behavior of linear mountain waves has been studied at length by previous authors and is summarized by Alaka (1960) and Smith (1979). If there is no shear in the mean cross-mountain wind speed, the behavior of linear hydrostatic mountain waves is governed by the following equation

$$\frac{\partial^2 \delta}{\partial z^2} + l^2 \delta = 0, \tag{39}$$

where $\delta$ is the displacement of a streamline from its height in the undisturbed flow, and $l$ is the Scorer parameter. If the atmosphere is isothermal, $l$ is constant,

$$l^2 = \frac{g}{c_p \bar{T} \bar{u}^2} - \frac{g^2}{4R^2 \bar{T}^2}. \tag{40}$$

We let the mountain contour be specified as

$$z_s(x) = \frac{ha^2}{x^2 + a^2} \tag{41}$$

and impose the linearized boundary condition $\delta(x, 0) = z_s$ at the surface. The remaining boundary conditions are specified by requiring that the disturbance vanish as $x \to -\infty$ and that all energy transport be directed away from the mountain as $z \to \infty$ (the radiation boundary condition). The solution to (39) subject to these boundary conditions is

$$\delta(x, z) = \left(\frac{\bar{\rho}}{\rho_0}\right)^{-1/2} ha \frac{a \cos lz - x \sin lz}{x^2 + a^2} \tag{42}$$

(for the full derivation see Alaka, 1960, or Smith, 1979). The perturbation horizontal and vertical velocities are obtained from the relations

$$u' = \frac{-\bar{u}}{\bar{\rho}} \frac{\partial \bar{\rho} \delta}{\partial z}, \quad w' = \bar{u} \frac{\partial \delta}{\partial x}. \tag{43}$$

Although the numerical model is neither linear nor hydrostatic, it should produce a steady solution which closely approximates (41) when the mountain is low (so the wave amplitude is essentially linear) and wide (so that the flow is nearly hydrostatic); i.e., whenever $Nh/\bar{u} \ll 1$ and $Na/\bar{u} \gg 1$. These requirements are satisfied in the following example, in which $\bar{T} = 250$ K, $\bar{u} = 20$ m s$^{-1}$, $a = 10$ km, and $h = 1$ m. The perturbation horizontal and vertical velocity fields calculated from (42) and (43) are displayed in Figs. 1a and 2a, and the corresponding fields obtained with the numerical model at $\bar{u}t/a = 60$ are shown in Figs. 1b and 2b. In this simulation, the computational domain contains 90 points in the horizontal and 80 levels in the vertical; the absorbing layer occupies the top 40 levels. The grid intervals are $\Delta x = 2$ km, $\Delta z = 200$ m; the large and small time steps are 20 and 4 s, respectively. Only the central portion of the computational domain is shown, in which the grid indices run from 20 to 70 in the horizontal and 1 to 40 in the vertical.

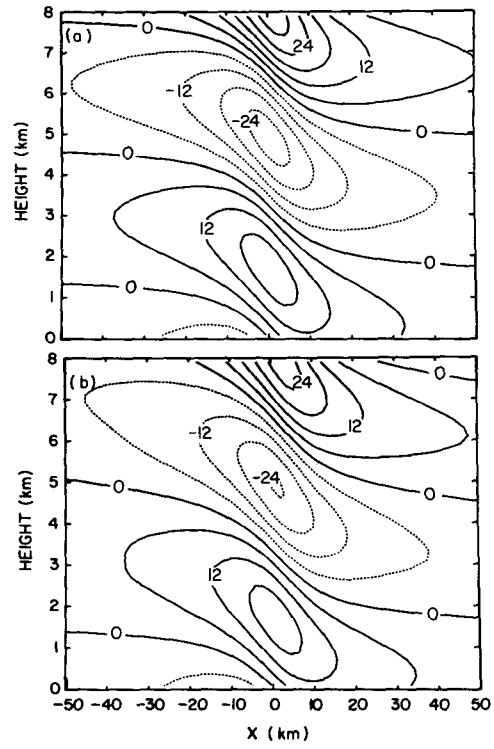


FIG. 1. (a) Steady state perturbation horizontal velocity (m s$^{-1}$) from the linear hydrostatic solution for a 1000 m high mountain. (b) Perturbation horizontal velocity (m s$^{-1}$) obtained by numerical simulation for a 1 m high mountain at $\bar{u}t/a = 60$; the perturbations have been amplified by 1000.

As evidenced in Figs. 1 and 2, the numerical and analytic solutions agree reasonably well. The vertical velocity fields match very closely, although the maxima and minima in the horizontal velocity field are somewhat underestimated by the numerical model. (The analytically and numerically computed streamlines, which are not shown, also agree very well.)

Mountain waves transport horizontal momentum vertically. The momentum flux

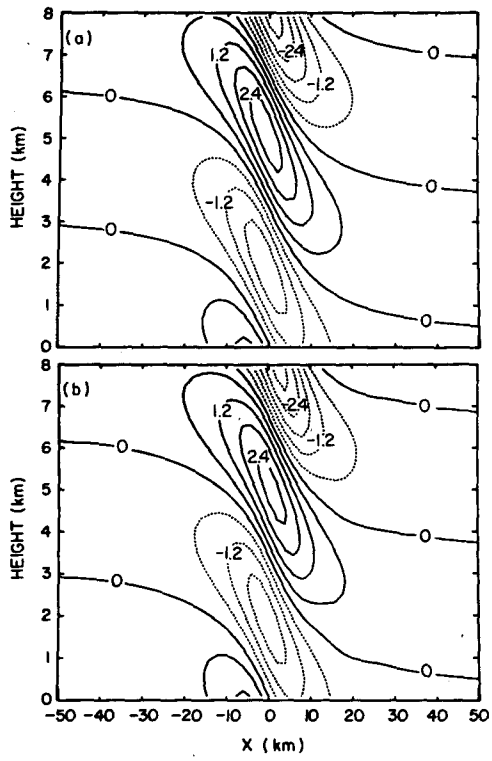


FIG. 2. As in Fig. 1, except that the fields plotted are vertical velocity (m $s^{-1}$).

$$M(z) = \int_{-\infty}^{\infty} \bar{\rho} u'w' dx \tag{44}$$

has important physical significance and is also a sensitive measure of error in the solution. Fig. 3 shows the vertical distribution of the numerically computed momentum flux at several nondimensional times $\bar{u}t/a$; the flux is normalized by the analytic linear hydrostatic value

$$M_H = -\frac{\pi}{4} \rho_0 N \bar{u} h^2, \tag{45}$$

where $\rho_0$ is the density at the surface. As the model approaches steady state, the flux becomes almost constant with height in the region below the absorbing layer, but remains a few percent below its linear steady state value. Klemp and Lilly (1980) have calculated the time dependent momentum flux profiles for the linear hydrostatic case in which a mean wind is introduced abruptly at $t = 0$. They found that at a height of one vertical wavelength (6.4 km in this case), the flux did not reach 95% of its steady state value until a nondimensional time of 35. As shown in Fig. 3, the flux is developing a little more slowly in the model. This is partly the result of the initialization procedure, in which the wind speed is gradually increased from zero to its mean upstream value over a nondimensional time of 5. However, even at $\bar{u}t/a = 60$, the flux at $z = 6.4$ km is still only 94% of its steady value. This residual vertical gradient in the flux is not due to any dissipation explicitly included in the model (turning off the fourth-order smoothing has a negligible impact on the flux).

On the whole, the behavior of the momentum flux, which as a second-order quantity is more sensitive to error than the velocity fields, appears satisfactory. The errors observed in this test case may be interpreted as a practical limit on the accuracy of the model's flux calculations.

### b. *Nonhydrostatic Long's solution*

In order to assess further the model's accuracy, we will consider a second test case in which nonlinear and nonhydrostatic effects play an important role. Long's equation (Long, 1953) may be applied to a compressible Boussinesq fluid (Raymond, 1972)

$$\frac{\partial^2 \delta}{\partial z^2} + \frac{\partial^2 \delta}{\partial x^2} + \frac{N^2}{\bar{u}^2} \delta = 0, \tag{46}$$

if the flow is steady and $\bar{u}$ and $N$ are constant, where $\delta$ is the displacement of a streamline from its undisturbed height, $\bar{u}$ the mean horizontal fluid velocity, and $N^2 = g/\theta_0 \partial\bar{\theta}/\partial z$ the Brunt–Väisälä frequency. The important property of (46) is that, although derived without making any small amplitude assumptions, it is a linear equation. Since it is linear, (46) can be easily solved; however, the boundary conditions remain difficult to apply.

The lower boundary condition

$$\delta(x, z_s) = z \tag{47}$$

cannot be linearized without invoking the hypothesis that the height of the obstacle is small. Long circum-

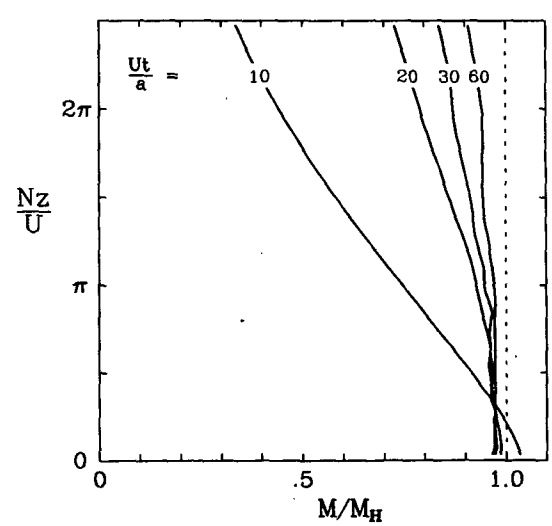


FIG. 3. Vertical flux of horizontal momentum, normalized by its linear hydrostatic value, at several nondimensional times $\bar{u}t/a$.

vented this by first solving (46) with a linearized boundary condition and then determining the finite amplitude mountain profile by solving (47) for $z_s$.

The radiation condition is again specified at the upper boundary. However, since it is formally valid only for linear waves, the application of the radiation condition to Long's equation cannot be rigorously defended. Nevertheless, there is reasonable justification for this choice, since, in the special case of Long's equation, the net effect of all nonlinear interactions is zero (Smith, 1977).

In this example, we consider the solution to (46) which is produced by the linearized lower boundary condition $\delta(x, 0) = z_s$, where $z_s$ is given by (41) with $h = 570$ m and $a = 2$ km,

$$\delta(x, z) = ha\,\mathrm{Re}\left\{\int_0^l \exp[i(kx + (l^2 - k^2)^{1/2}z) - kb]dk + \int_l^\infty \exp[ikx - kb - (k^2 - l^2)^{1/2}z]dk\right\}. \quad (48)$$

The actual terrain profile, determined implicitly by substituting (48) into (47), is similar in shape to the original profile, but its height is reduced to 500 m and its peak shifted slightly upstream. In addition, we choose $N = 0.01$ s$^{-1}$ and $\bar{u} = 10$ m s$^{-1}$. Then $\mathrm{Na}^*/\bar{u} \approx 2$ and $Nh^*/\bar{u} \approx 0.5$, where $a^*$ and $h^*$ denote the height and width of the implicitly determined mountain profile, so both nonhydrostatic and nonlinear effects should be significant in this example.

In applying Long's equation to the atmosphere, we assume that the flow is Boussinesq. Thus, for the purpose of this comparison, we slightly alter the numerical model to make it Boussinesq. This is accomplished by replacing $\theta_M$ by a constant mean $\theta_0$ in the coefficient of the pressure gradient terms in the momentum equations (10) and (11) and modifying the pressure equation (20) by replacing $\bar{c}$, $\bar{\rho}$, and $\bar{\theta}_M$ with constant mean values and setting $f_\pi$ to zero. The new form of the pressure equation is identical to the Boussinesq continuity equation except for the $\partial\pi/\partial t$ term which allows sound wave propagation. However, this term has little influence on the gravity wave modes and vanishes as the solution approaches steady state. [The artificial compressibility technique described by Chorin (1970) yields a similar equation.] In the numerical simulation, the computational domain contains 135 points in horizontal (with the mountain peak at the 45th grid point) and 72 levels in the vertical; the wave absorbing layer occupies the top 36 levels. The grid intervals are $\Delta x = 400$ m and $\Delta z = 250$ m; the large and small time steps are 8 and 1 s.

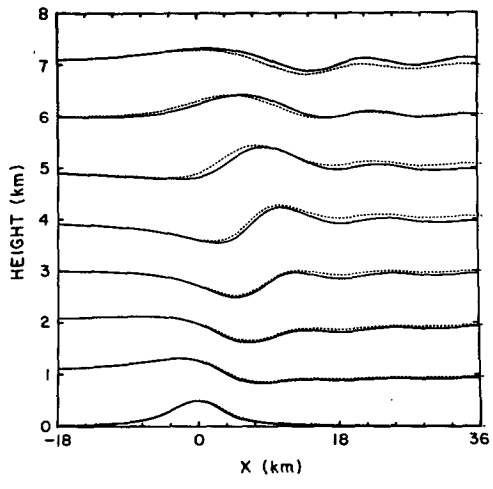


FIG. 4. Streamlines obtained from Long's solution (dashed lines), and by numerical simulation at $\bar{u}t/a = 40$ (solid lines).

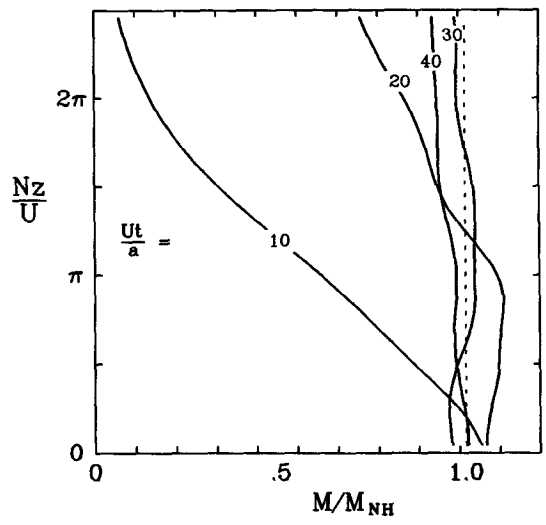


FIG. 5. Vertical flux of horizontal momentum, normalized by the analytic value from Long's solution, at several nondimensional times $\bar{u}t/a$.

The streamlines, obtained by evaluation of the integrals in (48), are compared with those produced by the numerical model at $\bar{u}t/a = 40$ in Fig. 4. (Only that portion of the domain for which the grid indices run from 20 to 90 in the horizontal and 1 and 32 in the vertical is shown in Fig. 4.) A slight divergence of the analytic and numerical streamlines can be observed at some levels downstream from the mountain; nevertheless the agreement between the two solutions is reasonably good. The time dependent behavior of the vertical distribution of the momentum flux is illustrated in Fig. 5. The fluxes have been normalized by their analytic value $M_{NH}$. Note that at a nondimensional time $\bar{u}t/a = 40$, the momentum flux profile computed by the numerical model agrees rather well with the steady-state analytic result.

### c. *Sensitivity tests*

Sensitivity tests suggest that changes in the initialization procedure have little influence on the numerical solution which develops at longer times, since the waves

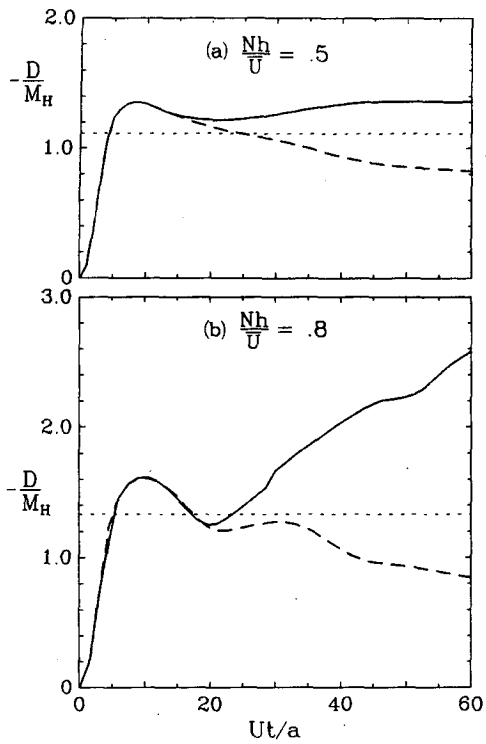


FIG. 6. Surface pressure drag, normalized by its linear hydrostatic value, as a function of time obtained from numerical simulations in which the bottom of a $1.5\lambda_z$ thick wave-absorbing layer is located at $1.25\lambda_z$ (solid line) or $1.5\lambda_z$ (dashed line), and $Nh/\bar{u}$ is (a) 0.5, or (b) 0.8.

are continuously forced by the terrain. The location of the lateral boundaries and the specific formulation of the lateral boundary conditions have a somewhat greater impact. The solutions are most sensitive to the inflow boundary conditions in highly nonlinear situations which produce significant upstream influence. This sensitivity can be minimized by locating the inflow boundary far upwind of the mountain (a distance of nine mountain half-widths proved to be acceptable in most situations). The influence of the outflow boundary on the numerical simulation depends on the types of waves present in the solution. Vertically propagating waves are not very sensitive to the downstream boundary, since they decay rapidly downwind of the mountain. In contrast, trapped waves may have considerable amplitude far downstream from the mountain, and consequently, they may be significantly affected by the downstream boundary. Errors are eventually produced at that boundary which propagate back upstream and degrade all large amplitude trapped wave solutions. In practice the onset of this problem can be delayed by moving the outflow boundary farther downstream.

The numerical solution is not strongly sensitive to the strength of the damping in the wave-absorbing layer, but it can be very sensitive to changes in the height at which the absorbing layer begins, i.e., the effective height of the upper boundary. This sensitivity increases as the amplitude of the waves entering the bottom of the absorbing layer increases. Numerical simulations of linear, weakly nonlinear, and trapped waves, which have little amplitude at the effective upper boundary, are not sensitive to changes in the height of that boundary.

Figure 6 illustrates the difference in the behavior of the surface pressure drag in two simulations with effective upper boundaries at 1.25 and 1.5 vertical wavelengths ($\lambda_z = 2\pi\bar{u}/N$), when the wave amplitude is moderately nonlinear (Fig. 6a) and strongly nonlinear (Fig. 6b). These simulations were conducted with the Boussinesq form of the model using 90 horizontal grid points and either 66 or 72 vertical grid levels; the absorbing layer occupied the top 36 levels (having a depth of $1.5\lambda_z$). The grid resolution was $\Delta x = 2$ km and $\Delta z = \lambda_z/24 = 250$ m); the large and small time steps were 25 and 5 s. The wind speed and stability were constant, with $\bar{u} = 10$ m s$^{-1}$ and $N = 0.01047$ s$^{-1}$. The mountain contour was specified according to (41) with $a = 10$ km; $h$ was chosen so that $Nh/\bar{u}$ is 0.5 in Fig. 6a and 0.8 in Fig. 6b.

The steady state hydrostatic solution was also calculated from Long's equation (Lilly and Klemp, 1979); the surface pressure drag associated with that solution is plotted in Fig. 6a,b for reference. Note that for this mountain shape, the steady Long's solution contains overturned streamlines (breaking waves) for $Nh/\bar{u} > 0.85$, so the situation simulated in Fig. 6b is indeed strongly nonlinear. As shown in both Figs. 6a and 6b, the solutions with differing domain depths are almost identical until a nondimensional time $\bar{u}t/a = 20$ (the model is initialized over the first five nondimensional time units). After $\bar{u}t/a = 20$, the shallow-domain solutions amplify, while the deep solutions decay. At $\bar{u}t/a = 60$, the solutions are still relatively similar in the moderately nonlinear case ($Nh/\bar{u} = 0.5$, Fig. 6a), but in the highly nonlinear case ($Nh/\bar{u} = 0.8$, Fig. 6b) they are very different. The shallow simulation contains a breaking wave and a feature resembling a hydraulic jump which propagates downstream from the mountain, whereas the deep simulation is qualitatively similar to Long's solution.

This sensitivity to the location of the upper boundary seems to be produced by an inadequate numerical approximation to the radiation boundary condition. However, it may be noted that the radiation boundary condition itself will not be correct if nonsteady, nonlinear mountain waves are generating downward-propagating waves through wave interactions. In such a case, the truncation of the numerical domain at any finite height with the application of the radiation condition would eliminate internally generated reflections from above that level and might produce the sensitivities observed in Fig. 6a,b.

The simulations of $Nh/\bar{u} = 0.8$ were repeated using a very deep wave-absorbing layer in which the thickness

was tripled to $4.5\lambda_z$, and the vertical gradient in the damping coefficient was correspondingly reduced by a factor of 3. The simulations are otherwise identical to those shown in Fig. 6b, except that the vertical grid resolution was halved to save computer time. As shown in Fig. 7, the sensitivity of the surface pressure drag to the location of the upper boundary has been drastically reduced (note that these simulations are run out longer than those in the shallow domain). Similar experiments, in which the depth of the domain is increased (to $4.5\lambda_z$) but the thickness of the wave absorbing layer is held constant (at $1.5\lambda_z$), also show some decrease in sensitivity. However, in the latter case, this is primarily due to an increase in the time required for errors at the upper boundary to propagate back down and degrade the solution. Although the sensitivity of the deep damping layer solutions is weak, as shown in Fig. 7, the surface pressure drag differs from that determined from Long's solution by 10–15%. The exact source of this error has not been determined but the lateral boundaries are the most likely candidates. Lilly and Klemp (1979) have obtained numerical solutions with an $\theta$ coordinate model which agree more closely with Long's solution for the case $Nh/\bar{u} = 0.74$. However, in those simulations the lateral boundaries were located at $\pm 72a$ (where $a$ is the mountain half-width) to remove all lateral boundary influences; by contrast, the boundaries in the current simulations are located much closer to the mountain at $\pm 9a$.

These sensitivity tests suggest that the accurate simulation of vertically propagating, highly nonlinear mountain waves requires a very thick wave absorbing layer. The sensitivity to changes in the height of "shallow" absorbing layers does not seem to be peculiar to this model; similar behaviors have been observed in the numerical models of Klemp and Lilly (1978) and Clark and Peltier (1977) although they use somewhat

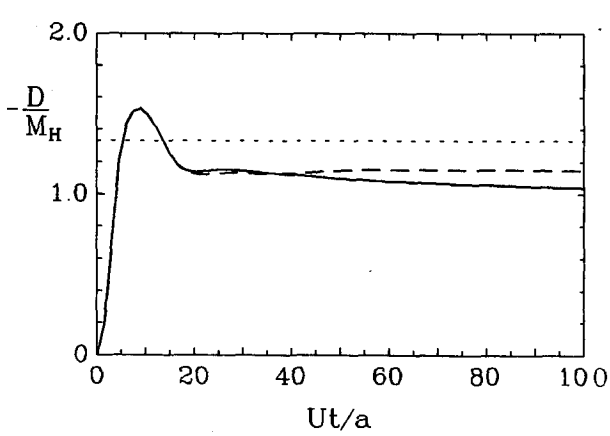


FIG. 7. As in Fig. 6 but in which the bottom of a $4.5\lambda_z$ thick wave-absorbing layer is located at $1.25\lambda_z$ (solid line) or $1.5\lambda_z$ (dashed line), and $Nh/\bar{u} = 0.8$.

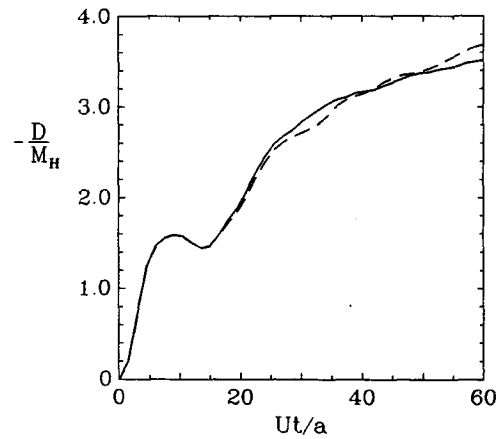


FIG. 8. As in Fig. 6b but in which the bottom of a $1.5\lambda_z$ wave absorbing layer is located at $1.25\lambda_z$ (solid line) or $1.5\lambda_z$ (dashed line), and a decrease in the mean wind speed produces a region of wave breaking in the computational domain.

different formulations for the wave absorber. In addition, when an entirely different numerical radiation boundary condition (Klemp and Durran, 1983) was used to replace the wave absorbing layer in this model, a similar sensitivity remained.

In most practical applications, it is simply not feasible to devote 80% of the numerical domain to the wave-absorbing layer. This difficulty can be avoided when simulating a real atmospheric flow by ensuring that the computational domain explicitly includes those regions which are primarily responsible for wave absorption or trapping. The effectiveness of this approach is illustrated in Fig. 8, which describes a situation identical to that in Fig. 6b except that the mean wind speed decreases linearly from 10 to 6 m $s^{-1}$ between the heights of 3 and 5 km, so that the local inverse Froude number ($Nh/\bar{u}$) increases with height from 0.8 to 1.3. In this case, the wave breaks as it enters the region of decreasing wind speed, and its energy is largely dissipated by mixing so that the disturbance which reaches the top of the domain has relatively low amplitude and can be properly radiated by a "shallow" ($1.5\lambda_z$ thick) absorbing layer. Note, however, that the low level structure of the insensitive solution is at least as nonlinear as that in the sensitive case (compare the surface wave drags in Figs. 6b and 8).

Boundary condition sensitivities aside, it is also important to explicitly include the region in which the waves are absorbed because it can have an important impact on the wave structure. As an example, note that the linear solutions to the cases shown in Figs. 6b and 8 should be identical in the layer between the ground and 3 km, since the mean Richardson number is large throughout the domain (Klemp and Lilly, 1975). However, as shown by the streamline fields in Fig. 9, the nonlinear solution is strongly influenced by the changes in the upper-level wind speed. Thus, it

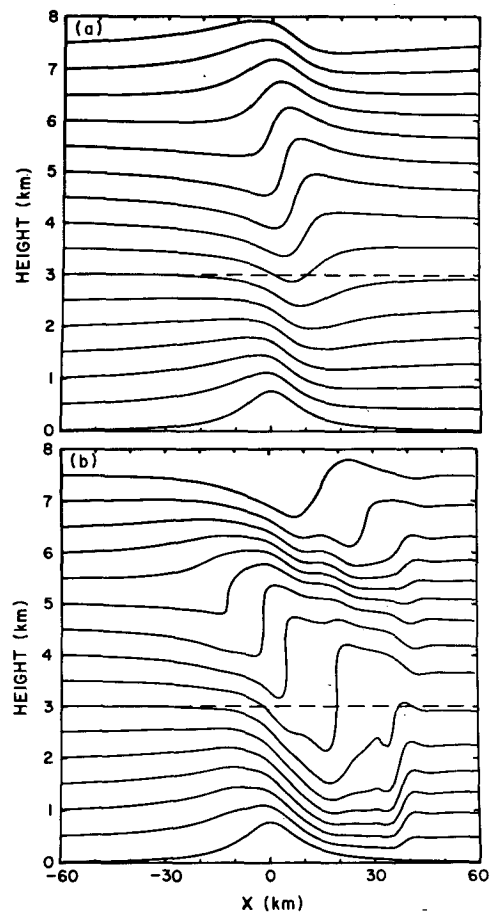


FIG. 9. Streamlines for two flows, which have identical linear solutions between the heights of 0 and 3 km, obtained from numerical simulations at $\bar{u}t/a = 40$. (a) $\bar{u} = 10$ m s$^{-1}$, constant with height; (b) $\bar{u}$ decreases gradually from 10 m s$^{-1}$ to 6 m s$^{-1}$ above a height of 3 km.

seems important to include the region of stratospheric wave breakdown in most simulations of actual mountain waves. In the Rocky Mountain region of the United States, this will generally require that the modeling region extend to a height of 15 to 20 km.

### *d. The 11 January 1972 windstorm in Boulder, Colorado*

We will conclude our discussion of the model verification with a simulation of the famous windstorm which occurred in Boulder, Colorado on 11 January 1972 (Lilly and Zipser, 1972; Lilly, 1978). Our primary intention is not to study the storm itself but to attempt to reproduce the large amplitude waves observed during that event and to compare results with the numerical simulation of Peltier and Clark (1979, denoted by PC). Although several investigators have simulated this storm, PC have performed the only nonhydrostatic simulation, so their results are most suitable for comparison with the current model.

We have chosen to simulate the 11 January 1972 case using a numerical grid and upstream atmospheric profile which match those used by PC as closely as possible. In our simulation, the computational domain contains 128 grid points in the horizontal and 83 grid levels in the vertical; the damping layer occupies the top 39 levels. The horizontal grid intervals are $\Delta x = 1000$ m and $\Delta z = 341$ m; the large and small time steps are 5 and 2.5 s. The mountain contour is specified by (41) with $a = 10$ km, $h = 2$ km, and the upstream wind speed and temperature profiles are specified as shown in Fig. 10. Except for the horizontal resolution which has been halved, and the time steps, the preceding parameters are identical to those used by PC.

The isentrope fields predicted by our model are displayed in Figs. 11a,b; at times $t = 4000$ and 8000 s, respectively. These may be compared with the results in PC which are reproduced in Figs. 11c,d for the times $t = 4160$ and 8000 s. The time dependent behavior of the surface wave drag computed by both models is compared in Fig. 12. Considering the many differences in numerical structure between the two models (they use different finite differencing, boundary condition schemes, and start-up procedures, and their equations are anelastic, ours contain sound waves), we observe that the agreement between the two simulations is remarkably good, and both models compare well with aircraft observations of the storm structure.

This simulation is not sensitive to changes in the height of the wave absorber, since the computational domain includes a region of wave breakdown and absorption in the lower stratosphere. We believe that these simulations are good representations of the actual windstorm event; however, they are not without some shortcomings. As evident in Fig. 12, the numerical

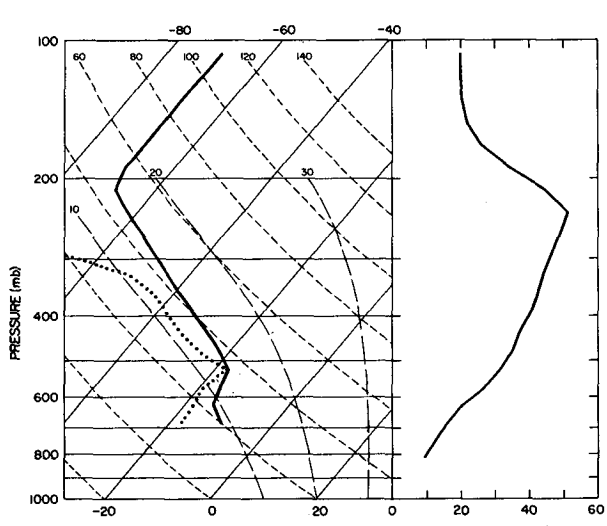


FIG. 10. Upstream sounding used by Peltier and Clark for the 11 January 1972 windstorm simulations. Moisture profile is from the 11 January 1200 GMT Grand Junction sounding.

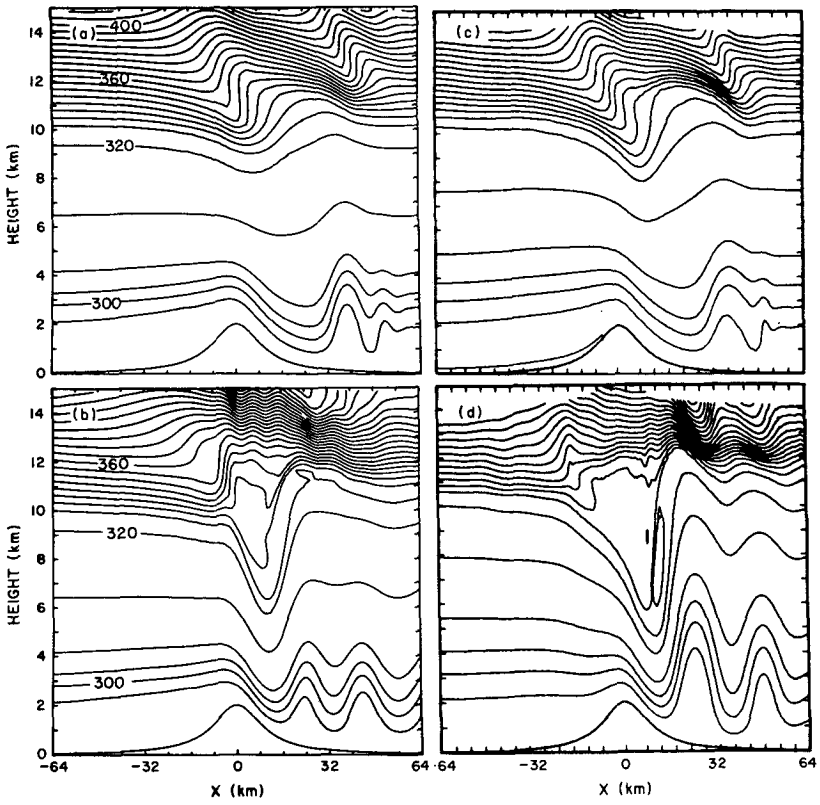


FIG. 11. Isentropes obtained by numerical simulation of the 11 January 1972 Boulder windstorm using this model at (a) $t$ = 4000 and (b) $t$ = 8000 s. Isentropes determined from the simulation of Peltier and Clark (1979) at (c) $t$ = 4180 and (d) 8000 s. Different isentropes are contoured by the different models.

solution is not steady, but is gradually amplifying. The actual windstorm was not completely steady, and some of the drift in the numerical solution may reflect that nonsteadiness. However, the tendency toward indefinite amplification shown in Fig. 12 is clearly nonphysical; it may reflect the absence of surface friction in the models.

## 4. Two examples which illustrate the effects of moisture on propagating mountain waves

In this section, we will discuss the influence of moisture on propagating mountain waves in two examples which demonstrate the utility of the model and illustrate the impact which moisture can have on nearly hydrostatic mountain waves.

### *a. The influence of moisture on a linear propagating wave*

The simplest situations in which to study the influence of moisture on mountain waves occur when the waves are hydrostatic and have small amplitude. If the Scorer parameter is constant with height and the terrain profile is specified by (41), the solution is again given by (42). In the first case discussed in Section 4a, the atmosphere was isothermal so that $l$ was exactly constant with height. This unrealistic assumption can be relaxed if the effects of compressibility on $l$ are neglected

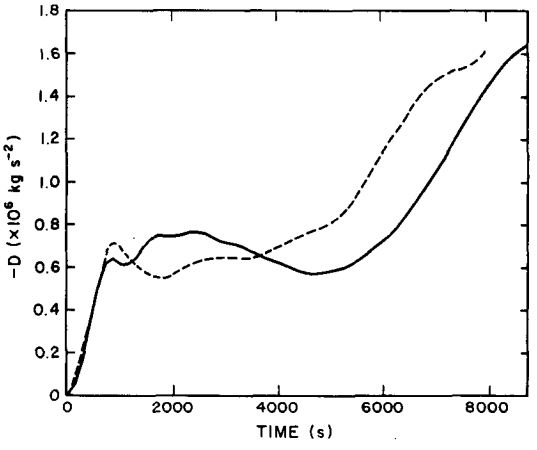


FIG. 12. Magnitude of the surface wave drag as a function of time, from this model (solid line) and from the simulation of Peltier and Clark (1979) (dashed line).

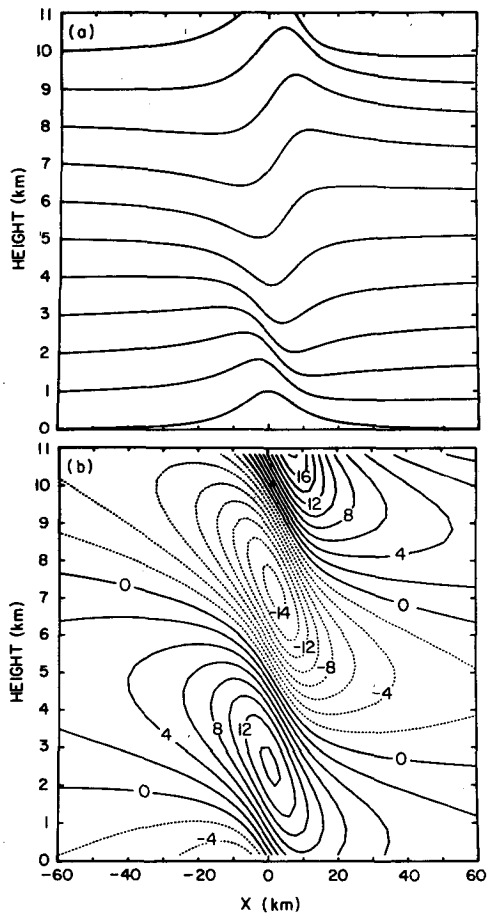


FIG. 13. (a) Streamlines and (b) horizontal velocities produced by a 1 m high mountain when RH = 0% upstream. The perturbations have been multiplied by 1000 for display; as such they constitute a linear numerical solution for a 1 km high mountain.

(usually a good approximation). Then the approximate Scorer parameter

$$l^2 = \frac{N^2}{\bar{u}^2} - \frac{\bar{u}_{zz}}{\bar{u}} \tag{49}$$

is constant with height in any atmosphere with uniform wind and stability.

Figure 13 shows the streamline and horizontal velocity fields computed by the model for a dry flow in which $N = 0.0132\ s^{-1}$ and $\bar{u} = 20\ m\ s^{-1}$. The mountain contour is specified by (41) with $h = 1$ m and $a = 10$ km. In this simulation the domain contains 90 points in the horizontal and 66 levels in the vertical; the wave absorbing layer occupies the top 33 levels. The grid intervals are $\Delta x = 2$ km, $\Delta z = 333$ m; the large and small time steps are 20 and 5 s. The model is run until the solution reaches a nearly steady state (20 000 to 30 000 s after start-up). Fig. 13 includes only the central portion of the domain, in which the grid indices run from 15 to 75 in the horizontal and 1 to 33 in the vertical. As in the first example in Section 4a, $Na/\bar{u} \gg 1$, $Nh/\bar{u} \ll 1$, so the model results are essentially linear and hydrostatic. The perturbation fields have been multiplied by 1000 for display; as such they represent the approximate linear solution for a 1 km high mountain.

Figures 14 and 15 show the waves produced in the same flow for cases where RH = 100% with 0.0 and 0.2 g $kg^{-1}$ of cloud upstream. No rain is allowed in these runs so condensation and evaporation are reversible. A comparison of Figs. 13, 14, and 15 shows that the moist waves are appreciably weaker than the dry wave. The differences in the horizontal wind speed maxima and minima are particularly pronounced. In an atmosphere with constant $N$ and $\bar{u}$, the horizontal wind speed perturbations are proportional to $N$, so it is reasonable to expect the reductions in effective stability which occur in saturated regions to have a strong impact on the horizontal wind speed.

The change in stability also has a large effect on the vertical wavelength, which in the case of constant $N$ and $\bar{u}$ is $2\pi\bar{u}/N$. In the dry case, the first vertical half-wavelength (the height at which the streamline contour is a mirror image of the mountain) is approximately

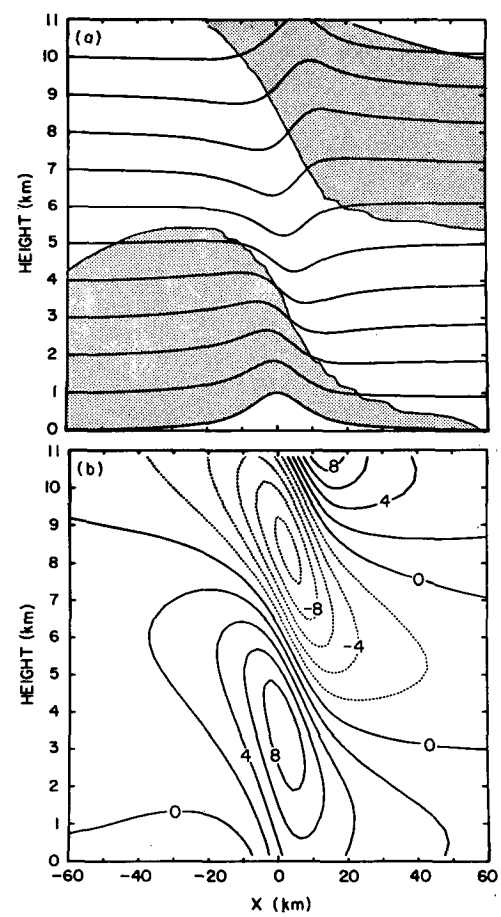


FIG. 14. (b) As in Fig. 13, except that RH = 100% in the upstream flow. Cloudy regions are shaded.

5 km; it increases to 6.5 and 7.5 km in the partially cloudy and everywhere cloudy cases. Klemp and Lilly (1975) have shown that linear hydrostatic waves experience strong amplification in multilayer atmospheres in which the total phase shift across the tropospheric layers is one-half vertical wavelength. The ability of moisture to alter the vertical wavelength should allow changes in humidity to tune or detune the tropospheric phase shift and thereby significantly modulate the wave response.

The vertical profile of the momentum flux associated with each of these waves is shown in Fig. 16. The momentum flux in the moist waves is less than half that in the dry wave; the weakest flux is produced by the partially saturated wave. Since there is no net heating in any of these examples, the fluxes are all approximately constant with height, in agreement with the results of Eliassen and Palm (1960).

The fluxes have been normalized by the exact expression for the momentum flux in a linear hydrostatic wave (45). Although (45) was derived for an atmosphere with constant Scorer parameter, it can also

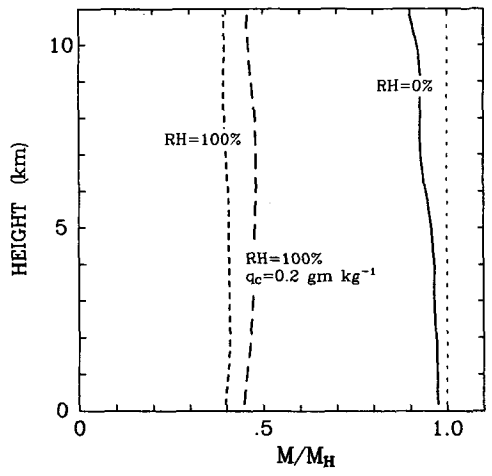


FIG. 16. Vertical flux of horizontal momentum, normalized by the dry linear hydrostatic value, produced by linear waves in three cases with different upstream humidity.

be applied in situations like the everywhere cloudy case, in which $l$ increases gradually with height so that upward propagating waves are neither trapped nor partially reflected by regions where the atmospheric structure changes rapidly. In this approach, the equivalent moist stability at the surface $N_m$ [see Durran and Klemp, 1982b and Eq. (A19)] is substituted for the dry stability in (45). In our example, the moist stability at the surface is 0.0062 s$^{-1}$, which yields an estimate for the momentum flux of $0.47M_H$. As shown in Fig. 16, the momentum flux determined from the model is in good agreement with that obtained analytically in both the dry ($1.0M_H$) and everywhere cloudy ($0.47M_H$) cases.

In the preceding small amplitude examples the clouds do not precipitate, so the microphysics are reversible and the practical effect of moisture is to decrease the stability in the saturated regions. In principle the moist flow could be calculated by replacing the clouds with regions of suitably reduced stability. Barcilon *et al.* (1979) have taken such an approach and found, in their linear calculations, that low level moisture could reduce the wave drag by up to 50%. Their estimate is consistent with the small amplitude results given here. We are not able to present a more complete, quantitative comparison with the calculations of Barcilon *et al.* (1979), because their assumption that both $N$ and $N_m$ are constant with height is not consistent with the actual stability structure in the atmosphere. That assumption may be reasonable in shallow clouds, but it is never strictly correct and is generally not appropriate in deep clouds.

### *b. The influence of moisture on the 11 January 1972 Boulder windstorm*

The simulation of the 11 January 1972 mountain wave event in Boulder, Colorado described in Section

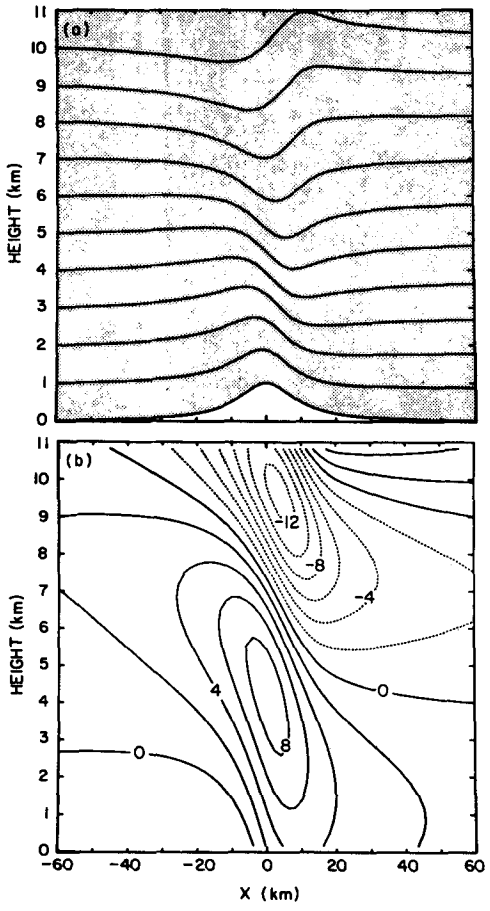


FIG. 15. As in Fig. 13, except that RH = 100% with 0.2 g kg$^{-1}$ of cloud in the upstream flow.

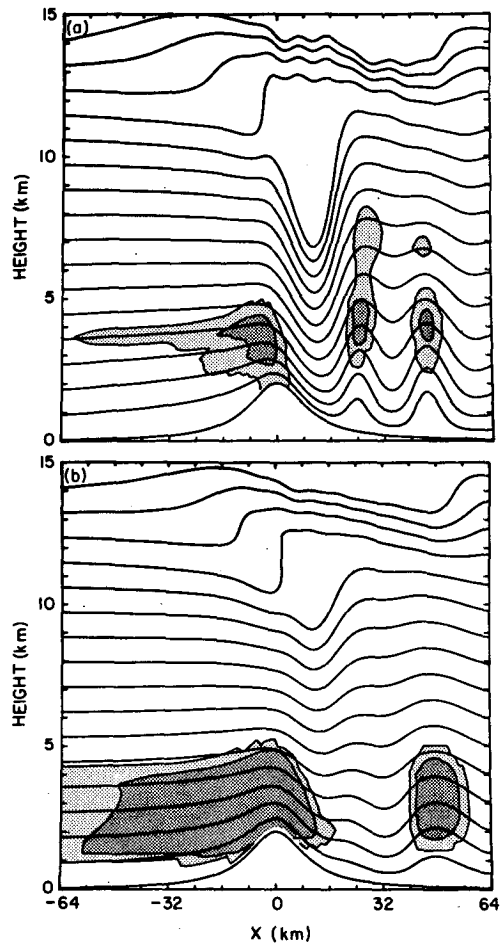


FIG. 17. Streamlines obtained by numerical simulation of the 11 January 1972 windstorm in which the upstream humidity (a) is determined from the Grand Junction sounding and (b) includes a cloud layer with 0.2 g kg$^{-1}$ of liquid water between 700 and 500 mb. Cloudy regions are shaded; dark shading represents liquid water concentrations exceeding 0.2 g kg$^{-1}$.

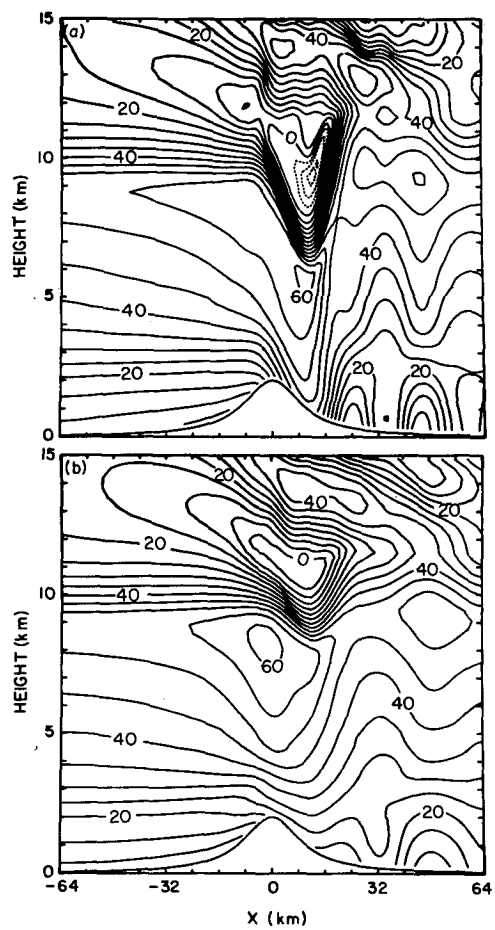


FIG. 18. As in Fig. 16, except that the fields plotted are the horizontal wind speed (m s$^{-1}$).

4d has been repeated with the moisture distribution reported in the 11 January 1200 GMT Grand Junction sounding included in the flow. The resulting streamlines and horizontal velocity field are shown in Figs. 17a and 18a; the time dependent behavior of the surface pressure drag is shown in Fig. 19. The moist solution resembles the completely dry solution discussed earlier (since they are so similar, the streamlines and horizontal velocity field from the dry simulation are not shown). The cloud distribution is also shown in Fig. 17a. The model clouds are similar, though somewhat larger than those actually observed during the windstorm (Lilly and Zipser, 1972).

The upstream humidity profile measured at Grand Junction is rather dry. Suppose that the Grand Junction sounding had included a saturated layer, containing 0.2 g kg$^{-1}$ of liquid water between 700 and 500 mb

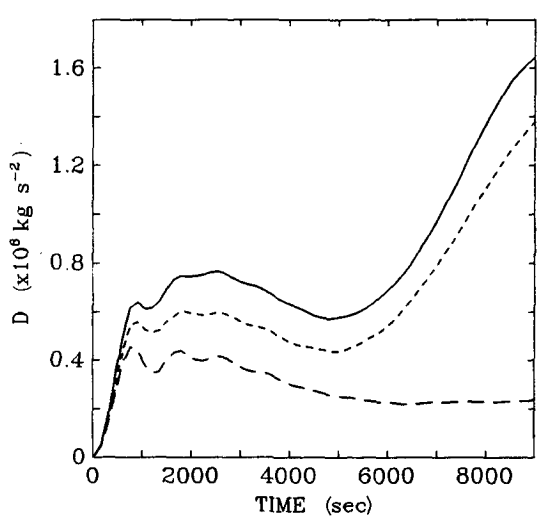


FIG. 19. Magnitude of the surface pressure drag as a function of time from the 11 January 1972 simulations when the upstream conditions were dry (solid line), contained the humidity observed in the Grand Junction sounding (short dashed line), and contained a cloud between 700 and 500 mb (long dashed line).

in the upstream flow. The influence of this very moist, but not unrealistic, humidity profile on the streamlines, horizontal velocity fields and surface pressure drag is illustrated in Figs. 17b, 18b and 19. As is evident, the additional moisture weakens the mountain wave considerably. The maximum downslope windspeed is reduced from almost 45 m $s^{-1}$ to less than 25 m $s^{-1}$ (Fig. 18); and the surface pressure drag, which shows no tendency toward amplification, is reduced by a factor of 6 at $t = 9000$ s (Fig. 19). Although the tropospheric wave response is much weaker in the very moist case, the wave amplitude above 12 km in the stratosphere is rather similar to that in the dry case. Note in particular that both solutions contain a breaking wave in the lower stratosphere, yet a strong tropospheric response is only produced in the low moisture case.

The lee side warming associated with the Alpine foehn is often attributed to the latent heat irreversibly released in the low level air which ascends the windward slope moist adiabatically and then descends dry adiabatically. However, in this instance, the effect of irreversible heating on the lee side temperature is dominated by dynamical processes. Precipitation occurs only in the very moist case (from the cap cloud at a maximum rate of 0.2 cm $h^{-1}$), yet the lee side temperatures are several degrees lower than those obtained in the drier, nonprecipitating flow. The most important factor which influences the lee temperatures is the wave amplitude which is larger in the drier case. A second simulation, in which rainwater was not allowed to form, produced results very similar to those obtained with rain, suggesting that (in this case) the irreversible heating associated with precipitation does not have a major impact on the wave structure. As noted by Smith and Lin (1982) the influence of precipitation on the flow dynamics can be much greater in tropical situations where the air holds more water vapor.

Perhaps it is not surprising that the addition of moisture reduces the wave amplitude in a situation where the dry atmosphere is already favorable for the generation of strong mountain waves. However, the results presented here, together with the previous studies of Barcilon *et al.* (1979) and Durran (1981), suggest that the presence of low level moisture does tend to decrease the wave response in a variety of situations. It may also be possible that the presence of moisture can amplify the wave response in cases which are otherwise unfavorable for the development of strong waves. According the linear theory of hydrostatic mountain waves presented by Klemp and Lilly (1975), such amplification may occur if the longer vertical wavelengths associated with saturated waves produce a phase shift across the troposphere which is closer to one-half vertical wavelength than the phase shift for the corresponding dry flow. We are continuing our research with this model in order to gain a more thorough understanding of the impact of precipitating and nonprecipitating clouds on the dynamics of vertically propagating mountain waves.

## 5. Summary

We have presented a detailed description of a two-dimensional, nonhydrostatic, compressible model designed to numerically simulate moist orographic flows. The model was found to reproduce known analytic solutions with reasonable fidelity. The numerical solutions did exhibit a strong sensitivity to the location of the upper boundary whenever highly nonlinear waves propagated into the absorbing layer. This sensitivity was eliminated by the use of a very deep wave absorbing layer (4.5 vertical wavelengths). The sensitivity was also removed if a wave breakdown (or trapping) region was explicitly included in the computational domain, so that the disturbance which actually reached the wave absorber was significantly weaker than that generated at low levels.

Most mountain waves which have large amplitudes in the troposphere may be expected to overturn somewhere in the lowest 10 km of the stratosphere. Thus, in most cases it is possible to explicitly include at least one region of wave breakdown and absorption in the numerical domain. Since the vertically propagating wave is not entirely dissipated at the first breakdown level, a radiation boundary condition must still be applied at the top of the model, but under these circumstances satisfactory performance can be achieved from a relatively thin absorbing layer.[4] In any event, the inclusion of the lowest wave breakdown level in the numerical domain is advisable since overturning can have a strong effect on the wave structure below.

The utility of the model has been demonstrated in two examples that illustrate how the presence of moisture can impact propagating mountain waves. In the first example, the strength of a linear dry mountain wave was reduced by approximately 50% when the upstream relative humidity was increased from 0 to 100%. The presence of additional moisture in the form of upstream clouds had little additional impact. In the second example, a dry simulation of the 11 January 1972 Boulder windstorm was insensitive to an increase in humidity equal to that actually observed in the Grand Junction sounding. However, a very wet but nevertheless realistic moisture distribution containing a cloud between 700 and 500 mb upstream, produced a dramatic reduction in the tropospheric wave amplitude. The lee slope warming was a strong function of the wave amplitude, so that even though precipitation and irreversible heating occurred only in the very moist case, the lee slope temperatures were warmer in the drier, nonprecipitating cases. A more comprehensive investigation of the effects of moisture on ver-

[4] The numerical radiation boundary condition proposed by Klemp and Durran (1983) is also effective and is considerably more efficient.

tically propagating mountain waves is currently in progress.

*Acknowledgments.* This research was sponsored in part by the NCAR Advanced Study Program and NASA Grant NSG-2010 to the MIT Department of Meteorology and Physical Oceanography.

APPENDIX

## Details of the Numerical Model

### 1. Grid structure

The model uses the standard staggered mesh shown in Fig. 20. Thermodynamic and moisture variables are all represented at a common grid point; velocity variables are displaced half a grid interval from that point. This arrangement improves the resolution in the pressure gradient and divergence terms without requiring a reduction in the large time step.

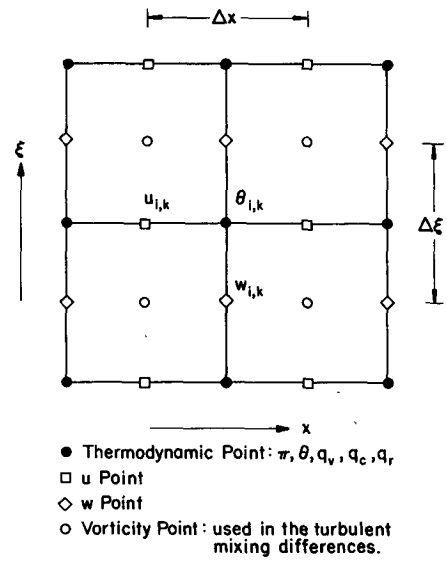


FIG. 20. Structure of the numerical grid.

### 2. Microphysics

The cloud microphysics are included through a Kessler parameterization in which moisture is divided into three categories: water vapor, cloud water (liquid water droplets with negligible fall speeds), and rain water (liquid water droplets with finite fall speeds). The microphysical terms in (4)–(7) are

$$M_\theta = -\frac{L}{c_p\bar{\Pi}}(\Delta + E_r), \tag{A1}$$

$$M_{q_v} = \Delta + E_r, \tag{A2}$$

$$M_{q_c} = -\Delta - A_r - C_r, \tag{A3}$$

$$M_{q_r} = \frac{1}{\bar{\rho}}\frac{\partial}{\partial z}(\bar{\rho}Vq_r) - E_r + A_r + C_r, \tag{A4}$$

where

$$\Delta = \begin{cases} 0, & q_v < q_{vs} \\ \dfrac{dq_{vs}}{dt}, & q_v \geq q_{vs}. \end{cases}$$

Here $L$ is the latent heat of vaporization, $E_r$ the evaporation of rain, $A_r$ and $C_r$ are the contributions of autoconversion and collection to raindrop development and growth, and $V$ the raindrop fall speed. The saturation mixing ratio, used to determine $\Delta$, is calculated from Teten's formula

$$q_{vs} = \frac{3.8}{\bar{p}}\exp\left(17.27\frac{\bar{\Pi}\theta - 273}{\bar{\Pi}\theta - 36}\right). \tag{A5}$$

The autoconversion and collection rates are given by the Kessler parameterization which assumes that the spectrum of raindrop radius follows a Marshall–Palmer distribution

$$A_r = k_1(q_c - a), \tag{A6}$$

$$C_r = k_2 q_c q_r^{0.875}. \tag{A7}$$

The autoconversion threshold and rate constants have nominal values of $a = 0.5$ g kg$^{-1}$, $k_1 = 0.001$ s$^{-1}$, $k_2 = 2.2$ s$^{-1}$. The evaporation of raindrops is given by

$$E_r = \frac{1}{\bar{\rho}}\frac{(1 - q_v/q_{vs})C(\bar{\rho}q_r)^{0.525}}{5.4 \times 10^5 + 2.55 \times 10^6/(\bar{p}q_{vs})}, \tag{A8}$$

where $C$ is the ventilation factor

$$C = 1.6 + 124.9(\bar{\rho}q_r)^{0.2046}\ [\text{s}^{-1}]. \tag{A9}$$

The raindrop fallspeed is approximated as

$$V = 36.34(\bar{\rho}q_r)^{0.1346}\left(\frac{\bar{\rho}}{\rho_0}\right)^{-1/2}\ [\text{m s}^{-1}]. \tag{A10}$$

In (A5)–(A10), $p$ is expressed in millibars, $\bar{\rho}$ in grams per cubic centimeter and $q_v$, $q_c$ and $q_r$ in grams per gram. Ice processes are not included in the model, since they are not critical to the investigation; they would significantly complicate the microphysical parameterization.

The microphysical forcing is calculated using a two-step procedure suggested by Soong and Ogura (1973). In the first step, the temperature and moisture variables are advected and diffused according to (4)–(7), except that the $M$ terms are ignored. Then, in the second step, (A1)–(A4) are evaluated using the results of step one.

Autoconversion, collection and the evaporation of rainwater are calculated as per (A6)–(A10). The evaporation of rain is limited by the amount of additional water vapor required to saturate the air. The rain water flux convergence is calculated from

$$\frac{\partial}{\partial\zeta}(\bar{\rho}Vq_r) = H\delta_{2\zeta}(\bar{\rho}Vq_r). \tag{A11}$$

At the lowest grid level, a one-sided difference is used; in order to maintain linear stability, it is lagged in time at $t - \Delta t$. Let the values of $\theta$, $q_v$ and $q_c$ at this point in the calculation be denoted by an asterisk.

In order to complete the evaluation of (A1)–(A3), the condensation rate, $-\Delta$, must be determined so that $\theta$ and $q_v$ are in equilibrium with $q_v^{t+\Delta t} = q_{vs}^{t+\Delta t}$. Of course any evaporation will be limited by $q_c^*$. We require the adjustment to proceed moist adiabatically; thus

$$\theta^{t+\Delta t} + \frac{L}{c_p\bar{\Pi}} q_v^{t+\Delta t} = \theta^* + \frac{L}{c_p\bar{\Pi}} q_v^*. \quad \text{(A12)}$$

Teten's formula for the saturation mixing ratio (A5) may be linearized about $\theta^*$ to obtain

$$q_{vs}^{t+\Delta t} = q_{vs}^*\left[1 + \frac{4093\bar{\Pi}}{(\bar{\Pi}\theta^* - 36)^2}(\theta^{t+\Delta t} - \theta^*)\right]. \quad \text{(A13)}$$

Then (A12) and (A13) are combined to obtain the desired expression for $\Delta$,

$$\Delta = -\max\left[\frac{q_v^* - q_{vs}^*}{1 + q_{vs}^*\dfrac{4093L}{c_p(\bar{\Pi}\theta^* - 36)^2}}, -q_c^*\right]. \quad \text{(A14)}$$

### 3. Subgrid scale mixing

When modeling phenomena on the scale of mountain lee waves, the effects of subgrid scale turbulence must be parameterized as a function of the larger scale flow. We employ a conventional first order closure formulation which depends on the relative strengths of stratification and shear (Lilly, 1962). Subgrid scale effects are introduced to the velocity field calculations through the terms $D_u$ and $D_w$

$$D_u = \frac{\partial}{\partial x}(K_M A) + \frac{\partial}{\partial z}(K_M B),$$

$$D_w = \frac{\partial}{\partial x}(K_M B) - \frac{\partial}{\partial z}(K_M A), \quad \text{(A15)}$$

where

$$A = \left(\frac{\partial u}{\partial x} - \frac{\partial w}{\partial z}\right), \quad B = \left(\frac{\partial u}{\partial z} + \frac{\partial w}{\partial x}\right), \quad \text{(A16)}$$

$$K_M = k^2\Delta x\Delta z(A^2 + B^2)^{1/2} \times\left[\max\left(1 - \frac{K_H}{K_M}\mathrm{Ri}, 0\right)\right]^{1/2}, \quad \text{(A17)}$$

$$\mathrm{Ri} = \begin{cases} \dfrac{N^2}{A^2 + B^2}, & \text{for } q_v < q_{vs} \\ \dfrac{N_m^2}{A^2 + B^2}, & \text{for } q_v = q_{vs}. \end{cases} \quad \text{(A18)}$$

Here Ri is the Richardson number, and

$$N_m^2 = g\left(1 + \frac{Lq_{vs}}{RT}\right)\left(1 + \frac{\epsilon L^2 q_{vs}}{c_p RT^2}\right)^{-1}\left(\frac{d\ln\theta}{dz} + \frac{L}{c_pT}\frac{dq_{vs}}{dz}\right) - g\left(\frac{d(q_v + q_c)}{dz}\right), \quad \text{(A19)}$$

and $\epsilon = 0.622$. The expression for the moist Brunt–Väisälä frequency $N_m$ is derived by Durran and Klemp (1982b) and is shown to be a satisfactory approximation to the exact expression. The subgrid scale mixing terms in the scalar equations are of the form

$$D_\phi = \frac{\partial}{\partial x}\left(K_H\frac{\partial\phi}{\partial x}\right) + \frac{\partial}{\partial z}\left(K_H\frac{\partial\phi}{\partial z}\right), \quad \text{(A20)}$$

where $\phi = \theta$, $q_v$, $q_c$, and $q_M$. In the model $k = 0.21$ (Deardorff, 1971) and $K_H/K_M = 3$ (Deardorff, 1972). This ratio of $K_H/K_M$ allows turbulent mixing to begin when Ri drops below ⅓, which is just slightly larger than the commonly accepted critical value for the stability of a shear flow, Ri = ¼.

The presence of the terrain transformation makes the evaluation of horizontal second derivatives in the subgrid scale mixing terms rather cumbersome. The finite differences are computed as follows:

$$A_1 = \delta_x u + G\overline{\delta_{2\zeta}u}^{x} - H\delta_\zeta w,$$

$$A_2 = \overline{\delta_{2x}u}^{\zeta} + G\delta_\zeta u - H\overline{\delta_{2\zeta}w}^{x}, \quad \text{(A21)}$$

$$B_1 = H\overline{\delta_{2\zeta}u}^{x} + \overline{\delta_{2x}w}^{\zeta} + G\delta_\zeta w,$$

$$B_2 = H\delta_\zeta u + \delta_x w + G\overline{\delta_{2\zeta}w}^{x}. \quad \text{(A22)}$$

The terms with subscript *1* are evaluated at thermodynamic points; those with subscript *2* at vorticity points. Continuing, we calculate

$$Def_1^2 = A_1^2 + B_1^2, \quad Def_2^2 = A_2^2 + B_2^2, \quad \text{(A23)}$$

$$\mathrm{Ri}_1 = \begin{cases} \dfrac{\alpha gH\delta_{2\zeta}\left(\theta + \dfrac{L}{c_p\bar{\Pi}}q_v\right)}{\left(\theta + \dfrac{L}{c_p\bar{\Pi}}q_v\right)(Def_1)^2} + gH\delta_{2\zeta}(q_v + q_c), & \text{saturated} \\ \dfrac{gH\delta_{2\zeta}\theta}{\theta(Def_1)^2}, & \text{unsaturated}, \end{cases} \quad \text{(A24)}$$

$$\mathrm{Ri}_2 = \begin{cases} \dfrac{\alpha g H \delta_\zeta \overline{\left(\theta + \dfrac{L}{c_p \bar{\Pi}} q_v\right)}^{x}}{\overline{\left(\theta + \dfrac{L}{c_p \bar{\Pi}} q_v\right)}^{x\zeta} (Def_2)^2} + g H \overline{\delta_\zeta (q_v + q_c)}^{x}, & \text{saturated} \\ \dfrac{g H \overline{\delta_\zeta \theta}^{x}}{\overline{\bar{\theta}^{x\zeta}} (Def_2)^2}, & \text{unsaturated,} \end{cases} \tag{A25}$$

$$\alpha(z) = \left(1 + \frac{L \bar{q}_{vs}}{R \overline{\bar{\Pi}\bar{\theta}}}\right)\left(1 + \frac{\epsilon L^2 \bar{q}_{vs}}{c_p R (\overline{\bar{\Pi}\bar{\theta}})^2}\right)^{-1}. \tag{A26}$$

The saturated form is used whenever $q_c > 0$ at all points involved in the calculation. Then,

$$K_{M_1} = k^2 \Delta x \Delta \zeta Def_1 (\max(0, 1 - 3\,\mathrm{Ri}_1))^{1/2},$$

$$K_{M_2} = k^2 \Delta x \Delta \zeta Def_2 (\max(0, 1 - 3\,\mathrm{Ri}_2))^{1/2}, \tag{A27}$$

and finally,

$$D_u = \delta_x (K_{M_1} A_1) + G \delta_\zeta (K_{M_2} A_2) - H \delta_\zeta (K_{M_2} B_2), \tag{A28}$$

$$D_w = \delta_x (K_{M_2} B_2) + G \delta_\zeta (K_{M_1} B_1) - H \delta_\zeta (K_{M_1} A_1). \tag{A29}$$

The mixing terms for the scalar variables are derived from $K_{M_1}$,

$$K_H = 3 K_{M_1}. \tag{A30}$$

Let

$$\begin{aligned} R &= \overline{K_H}^{x} (\delta_x \phi + G \overline{\delta_{2\zeta} \phi}^{x}), \\ S &= \overline{K_H}^{\zeta} (\overline{\delta_{2x} \phi}^{\zeta} + G \delta_\zeta \phi), \\ T &= \overline{K_H}^{\zeta} \delta_\zeta \phi. \end{aligned} \tag{A31}$$

Then

$$D_\phi = \delta_x R + G \delta_\zeta S + H^2 \delta_\zeta T. \tag{A32}$$

## 4. Large time step differencing

The right-hand sides of the momentum and continuity equations, with the coordinate transformation included, are

$$f_u = \frac{-u}{3}(4\delta_{2x} u - \delta_{4x} u) - \overline{(\bar{u}^{\zeta} G + H \bar{w}^{x}) \delta_\zeta u}^{\zeta} - c_p (\bar{\theta}_M^{x} - \overline{\theta_{M_0}}^{x})(\delta_x \pi + \overline{G \delta_{2\zeta} \pi}^{x}) + D_u, \tag{A33}$$

$$f_w = \frac{-\overline{\bar{u}^{x}}^{\zeta}}{3}(4\delta_{2x} w - \delta_{4x} w) - (\overline{\bar{u}^{x}}^{\zeta} G + H w) \delta_{2\zeta} w + (\bar{\theta}_M^{\zeta} - \bar{\theta}_{M_0}^{\zeta})\left(\frac{g}{\bar{\theta}_{M_0}^{\zeta}} - c_p H \delta_\zeta \pi\right) + D_w, \tag{A34}$$

$$f_\pi = \overline{-u \delta_x \pi}^{x} - \overline{(\bar{u}^{x\zeta} G + H w) \delta_\zeta \pi}^{\zeta} - \frac{R}{c_p} \pi (\delta_x u + G \overline{\delta_{2\zeta} u}^{x} + H \delta_\zeta w) + \frac{\bar{c}^2}{c_p \theta_{v0}}\left[\frac{M_\theta + D_\theta}{\theta} + \frac{0.61(M_{q_v} + D_{q_v})}{1 + 0.61 q_v}\right]. \tag{A35}$$

In the above, $\theta_{M_0}$ is the undisturbed value of $\theta_M$ along a constant $z$ surface (denoted $\bar{\theta}_M$ in earlier equations). Since the operator $\overline{(\ )}^{x}$ averages along a constant $\zeta$ surface, $\overline{\theta_{M_0}}^{x} \neq \theta_{M_0}$. In practice, the terms in (A33) and (A34) involving the pressure gradient, and the entire $f_\pi$ expression may be omitted with only minor effect on the solution; in fact, they are omitted in the three-dimensional cloud model of Klemp and Wilhelmson (1978). They are included in this model since the computational cost is not prohibitive, and their inclusion makes the finite difference equations formally equivalent to the full Navier–Stokes equations.

The scalar advection equations are all differenced identically

$$\delta_{2t} \phi = \frac{-\bar{u}^{x}}{3}(4\delta_{2x} \phi - \delta_{4x} \phi) - \overline{(\bar{u}^{x\zeta} G + H w) \delta_\zeta \phi}^{\zeta} + M_\phi + D_\phi. \tag{A36}$$

The small and large time steps are meshed as follows. The scalar equations for $\theta$, $q_v$, $q_c$ and $q_r$ are stepped from $t - \Delta t$ to $t + \Delta t$ by a single leapfrog step. The functions $f_u$, $f_w$ and $f_\pi$ are evaluated at the central time level $t$. Finally, the $u$, $w$, and $\pi$ fields are stepped forward from $t - \Delta t$ to $t + \Delta t$ with forward time differencing on the small time step. The total number of small time steps is $2\Delta t/\Delta \tau$.

## REFERENCES


Alaka, M. A., Ed., 1960: *The Airflow over Mountains.* WMO Tech. Note 34, 135 pp. [Available from UNIPUB].

Asselin, R., 1972: Frequency filter for time integrations. *Mon. Wea. Rev.*, **100**, 487–490.

Barcilon, A., J. C. Jusem and P. G. Drazin, 1979: On the two-dimensional hydrostatic flow of a stream of moist air over a mountain ridge. *Geophys. Astrophys. Fluid Dyn.*, **13**, 125–140.

——, —— and S. Blumsack, 1980: Pseudo-adiabatic flow over a

two dimensional ridge. *Geophys. Astrophys. Fluid Dyn.*, **16**, 19–33.

Chorin, A. J., 1970: Numerical solution of incompressible flow problems. *Studies in Numerical Analysis, 2: Numerical Solutions of Nonlinear Problems*, J. M. Ortega and W. C. Rheinbolt, Eds., SIAM, 143 pp.

Clark, T. L., 1977: A small scale dynamic model using a terrain following coordinate transformation. *J. Comput. Phys.*, **24**, 186–215.

——, 1979: Numerical simulations with a three-dimensional cloud model. Lateral boundary condition experiments and multicellular severe storm simulations. *J. Atmos. Sci.*, **36**, 2191–2215.

——, and W. Peltier, 1977: On the evolution and stability of finite amplitude mountain waves. *J. Atmos. Sci.*, **34**, 1715–1730.

Deardorff, J. W., 1971: On the magnitude of the subgrid scale eddy coefficient. *J. Comput. Phys.*, **7**, 120–133.

——, 1972: Numerical investigation of neutral and unstable planetary boundary layers. *J. Atmos. Sci.*, **29**, 91–115.

Durran, D. R., 1981: The effects of moisture on mountain lee waves. Ph.D. thesis, MIT. [NTIS PB82156621]

——, and J. B. Klemp, 1982a: The effects of moisture on trapped mountain lee waves. *J. Atmos. Sci.*, **39**, 2490–2506.

——, and ——, 1982b: On the effects of moisture on the Brunt–Väisälä frequency. *J. Atmos. Sci.*, **39**, 2152–2158.

Eliassen, A., and E. Palm, 1960: On the transfer of energy in stationary mountain waves. *Geofis. Publ.*, **22**, 1–23.

Fraser, A. B., R. C. Easter and P. V. Hobbs, 1973: A theoretical study of the flow of air and fallout of solid precipitation over mountainous terrain. Part I: Airflow model. *J. Atmos. Sci.*, **30**, 801–812.

Gal-Chen, T., and R. Somerville, 1975: On the use of a coordinate transformation for the solution of the Navier–Stokes equations. *J. Comput. Phys.*, **17**, 209–228.

Klemp, J. B., and D. K. Lilly, 1975: The dynamics of wave-induced downslope winds. *J. Atmos. Sci.*, **32**, 320–339.

——, and ——, 1978: Numerical simulation of hydrostatic mountain waves. *J. Atmos. Sci.*, **35**, 78–106.

——, and R. Wilhelmson, 1978: The simulation of three-dimensional convective storm dynamics. *J. Atmos. Sci.*, **35**, 1070–1096.

——, and D. K. Lilly, 1980: Mountain waves and momentum flux. GARP Pub. Ser. 23, *Orographic Effects in Planetary Flows*, ICSU/WMO, 450 pp.

——, and D. R. Durran, 1983: An upper boundary condition permitting internal gravity wave radiation in numerical mesoscale models. *Mon. Wea. Rev.* **111**, 430–444.

Lalas, D. P., and F. Einaudi, 1974: On the correct use of the wet adiabatic lapse rate in the stability criteria of a saturated atmosphere. *J. Appl. Meteor.*, **13**, 318–324.

Lilly, D. K., 1962: On the numerical simulation of buoyant convection. *Tellus*, **14**, 148–172.

——, 1978: A severe downslope windstorm and aircraft turbulence event induced by a mountain wave. *J. Atmos. Sci.*, **35**, 59–77.

——, and E. J. Zipser, 1972: The front range windstorm of 11 January 1972—A meteorological narrative. *Weatherwise*, **25**, 56–63.

——, and J. B. Klemp, 1979: The effects of terrain shape on nonlinear hydrostatic mountain waves. *J. Fluid Mech.*, **95**, 241–261.

Long, R. R., 1953: Some aspects of the flow of stratified fluids. I: A theoretical investigation. *Tellus*, **5**, 42–58.

Miller, M. J., and A. J. Thorpe, 1981: Radiation conditions for the lateral boundaries of limited-area numerical models. *Quart. J. Roy. Meteor. Soc.*, **107**, 615–628.

Orlanski, I., 1976: A simple boundary condition for unbounded hyperbolic flows. *J. Comput. Phys.*, **21**, 251–269.

Peltier, W. R., and T. L. Clark, 1979: The evolution and stability of finite-amplitude mountain waves. Part II: Surface wave drag and severe downslope windstorms. *J. Atmos. Sci.*, **36**, 1498–1529.

Raymond, D. J., 1972: Calculation of airflow over an arbitrary ridge including diabatic heating and cooling. *J. Atmos. Sci.*, **29**, 837–843.

Smith, R. B., 1977: The steepening of hydrostatic mountain waves. *J. Atmos. Sci.*, **34**, 1634–1654.

——, 1979: The influence of mountains on the atmosphere. *Advances in Geophysics*, Vol. 21, Academic Press, 87–230.

——, and Y. L. Lin, 1982: The addition of heat to a stratified airstream with application to the dynamics of orographic rain. *Quart. J. Roy. Meteor. Soc.*, **108**, 353–378.

Soong, S-T., and Y. Ogura, 1973: A comparison between axi-symmetric and slab-symmetric cumulus cloud models. *J. Atmos. Sci.*, **30**, 879–893.